

# Resolving flows around black holes: numerical technique and applications

Michael Curtis<sup>1\*</sup>, Debora Sijacki<sup>1</sup>

<sup>1</sup> *Institute of Astronomy and Kavli Institute for Cosmology, University of Cambridge, Madingley Road, Cambridge CB3 0HA, UK*

1 March 2024

## ABSTRACT

Black holes are believed to be one of the key ingredients of galaxy formation models, but it has been notoriously challenging to simulate them due to the very complex physics and large dynamical range of spatial scales involved. Here we address a significant shortcoming of a Bondi-Hoyle-like prescription commonly invoked to estimate black hole accretion in cosmological hydrodynamic simulations of galaxy formation, namely that the Bondi-Hoyle radius is frequently unresolved. We describe and implement a novel super-Lagrangian refinement scheme to increase, adaptively and ‘on the fly’, the mass and spatial resolution in targeted regions around the accreting black holes at limited computational cost. While our refinement scheme is generically applicable and flexible, for the purpose of this paper we select the smallest resolvable scales to match black holes’ instantaneous Bondi radii, thus effectively resolving Bondi-Hoyle-like accretion in full galaxy formation simulations. This permits us to not only estimate gas properties close to the Bondi radius much more accurately, but also allows us to improve black hole accretion and feedback implementations. We thus devise a more generic feedback model where accretion and feedback depend on the geometry of the local gas distribution and where mass, energy and momentum loading are followed simultaneously. We present a series of tests of our refinement and feedback methods and apply them to models of isolated disc galaxies. Our simulations demonstrate that resolving gas properties in the vicinity of black holes is necessary to follow black hole accretion and feedback with a higher level of realism and that doing so allows us to incorporate important physical processes so far neglected in cosmological simulations.

**Key words:** methods: numerical - black hole physics - cosmology: theory

## 1 INTRODUCTION

Growing observational evidence indicates that supermassive black holes reside in the centres of the majority of galaxies, including our own Milky Way. Observed scaling relations between the mass of black holes and the properties of the host galaxy bulge such as its mass, luminosity and velocity dispersion (e.g. Kormendy & Richstone 1995; Magorrian et al. 1998; Ferrarese & Merritt 2000; Gebhardt et al. 2000; Marconi & Hunt 2003; Gültekin et al. 2009; Kormendy & Ho 2013; McConnell & Ma 2013) suggest that the evolution of the central black holes and the host galaxies are closely linked. However, the extent to which the formation and growth of black holes impacts the galaxy formation process is not fully understood.

More direct evidence for the effects of black holes comes from recent observations of active galactic nuclei (AGN)-driven winds (e.g. Pounds et al. 2003; Sturm et al. 2011;

Maiolino et al. 2012; Veilleux et al. 2013; Ciccone et al. 2014; Genzel et al. 2014; Tombesi et al. 2015), indicating that AGN activity is affecting host galaxies by, for example, expelling large amounts of material at thousands of  $\text{km s}^{-1}$ . Moreover, in massive galaxies residing in group and cluster environments, a large body of X-ray studies (see e.g. Fabian et al. 2006; Forman et al. 2007, for two well studied examples) indicates that black hole-launched jets directly interact with the surrounding medium, heating it and thus suppressing star formation in the central galaxy. The umbrella term for these processes is ‘feedback’ (for a recent review see Fabian 2012), and this is understood to result from accretion of matter on to the black hole and the subsequent release of energy (Lynden-Bell 1969).

Since the mutual interaction between black holes and their host galaxies became apparent, it has become necessary to understand the accretion processes involved in order to answer many open questions in the field, including where the black hole–host relations come from, and the role AGN feedback plays in the quenching of star formation and in the

\* E-mail: mc636@ast.cam.ac.uk

evolution of galaxy morphologies. Various models have been proposed to describe the physics of black hole accretion and feedback analytically (e.g. Silk & Rees 1998; Fabian 1999; King 2005). Such models have generally been successful in explaining the black hole mass – stellar bulge velocity relationship (the so-called  $M_{\text{BH}} - \sigma$  relationship). They are, however, inevitably forced into making simplifying assumptions, such as spherical geometry, lack of treatment of concurrent star formation and large scale cosmological inflows of gas, that might seriously hinder their predictive power (see recent work by Costa et al. 2014). It is worth noting that accretion is not only coupled to the gas hydrodynamics, which is highly non-linear and complex, but also to the gravitational torques occurring on a large range of scales which are also difficult to describe analytically.

There is clear motivation, then, for including an accurate treatment of black hole growth and feedback in cosmological hydrodynamic simulations of galaxy formation and there have been many studies to this effect over the past 10 years (e.g. Di Matteo et al. 2005; Kawata & Gibson 2005; Springel et al. 2005; Sijacki et al. 2007; Booth & Schaye 2009; Debuhr et al. 2011; Power et al. 2011; Choi et al. 2012; Dubois et al. 2012). These models have to overcome the numerous computational and theoretical challenges associated with simulating AGN physics. First, and perhaps most importantly, the spatial scales involved span a massive range. If even a basic statistical sample of galaxies is to be achieved then a simulation domain must cover tens to hundreds of mega-parsecs (Mpc). This should be contrasted with the Schwarzschild radius for a supermassive black hole – for a mass of  $10^7 M_{\odot}$ ,  $r_s \approx 10^{-6}$  pc: a dynamic range that spans 14 orders of magnitude.

Thus if we want to study the impact of AGN on galaxies in full cosmological volumes, directly resolving the region of accretion is computationally infeasible and will continue to be so for a number of years. Furthermore, even if we could achieve the resolution necessary, the physics that governs accretion is poorly understood. To overcome this, numerical simulations that include AGN physics must adopt so-called sub-grid models. These algorithms track the unresolved physical processes that are ultimately expected to impact the simulations on large scales. In the case of AGN, these prescriptions define the changes in the physical properties of the black holes within the simulation, including how they accrete mass from the surrounding gas, how they are advected with the fluid flow, and how they deposit mass, energy and momentum back into the surrounding medium.

Many sub-grid techniques have been proposed and implemented in previous works (e.g. see a recent comparison study by Wurster & Thacker 2013), but there are essentially two main strategies. The first is to allow black holes to swallow particles or cells that come within a certain distance of them. Whilst this has the benefit that it does not require any further approximation, it has the downside that it is highly stochastic, causing the black hole mass to grow in discontinuous jumps as particles randomly fly close enough to be swallowed. Furthermore, there is no reason to expect such an accretion rate to be reliable at the typical resolution of current simulations.

The second approach to quantifying the gas accretion is to parameterize an accretion rate in terms of the local gas properties. Such a rate may be theoretically motivated,

or may be a parameterization from higher resolution ‘zoom-in’ simulations of smaller spatial scales. Perhaps the most commonly used theoretical rate is a Bondi-Hoyle-Lyttleton approach (Bondi 1952a), which adopts the simple formula

$$\dot{M}_{\text{B}} = \frac{4\pi G^2 M_{\text{BH}}^2 \rho_{\infty}}{(c_{\infty}^2 + v^2)^{3/2}}, \quad (1)$$

where  $M_{\text{BH}}$  is the mass of the black hole,  $\rho_{\infty}$  and  $c_{\infty}$  are the gas density and sound speed at infinity and  $v$  is the relative velocity between the black hole and the gas at infinity. Whilst elegant and easy to implement numerically, this approach also has a number of drawbacks.

First, for the Bondi calculation to be accurate, we require that the fluid be resolved at the Bondi-Hoyle radius<sup>\*</sup>

$$r_{\text{B}} = \frac{GM_{\text{BH}}}{c_{\infty}^2 + v^2}, \quad (2)$$

which is not the case, either for the vast majority of cosmological simulations, or for idealized test problems in the past literature.

Secondly, the Bondi rate ignores the rotation of the gas, which is likely to be very important. Gas with enough angular momentum will circularize before reaching the inner most stable orbit, forming an accretion disc and thus possibly slowing the rate at which such matter can fall on to the black hole. There have been several studies that have studied gas angular momentum near supermassive black holes in galaxy formation simulations (see e.g. Levine et al. 2010; Hopkins & Quataert 2011) or that have directly attempted to account for the angular momentum within an accretion rate prescription (e.g. Krumholz et al. 2005; Power et al. 2011; Anglés-Alcázar et al. 2013; Rosas-Guevara et al. 2015). These attempts face a number of key challenges: gas orbits must be accurately followed to robustly measure the angular momentum of the accretion flow on resolvable scales, whilst assumptions about the properties of the (innermost) accretion disc need to be made – in particular, the nature and magnitude of the viscous processes that drive the evolution of such discs. The gravitational instability of accretion discs leading to fragmentation (King & Pringle 2007) and possibly star formation and stellar feedback add yet another non-trivial layer of complexity.

Furthermore, the Bondi-Hoyle rate ignores several other effects, such as the impact of a non-uniform, turbulent gas flow (Krumholz et al. 2006). In this case, the deviation from the classic formula is less obvious, as for higher Mach number flows the accretion rate may be significantly increased, but such an enhancement can be offset by the vorticity of the flow. Additionally, in a regime where cooling is efficient, gas may be in free fall at large distances from the black hole leading to a significantly different outcome with respect to the standard Bondi-Hoyle rate (Hobbs et al. 2012).

Despite these limitations, the Bondi-Hoyle approach is still widely adopted in cosmological simulations. The extent to which the simulated accretion on to the black holes may deviate from reality is, so far, unclear, since the other key element in our models of black hole growth – the injection

<sup>\*</sup> Note that in the absence of the relative velocity term this simplifies to the Bondi radius  $r_{\text{B}} = \frac{GM_{\text{BH}}}{c_{\infty}^2}$ , which we will use throughout the paper.

and coupling of feedback to the surrounding gas - is also poorly constrained. Understanding both the feedback and the accretion together is fundamental - if the feedback is sufficient to shut off accretion then the black holes may enter a period of self-regulation, rendering the precise details of the accretion rate less important.

The goal of this paper is to tackle the first of these shortcomings, the unresolved Bondi-Hoyle radius, which is inherent in the current use of Bondi accretion in cosmological simulations. To this end we present a new modelling technique that enables us to resolve, 'on-the-fly' and adaptively, the gas surrounding black hole particles in a super-Lagrangian fashion. We use this technique to improve our estimation of the fluid properties local to the black hole, which we then use to compute the Bondi-Hoyle-like accretion more accurately. Our modelling technique has the potential to tackle additional shortcomings of the Bondi-Hoyle model, such as the need to consider the angular momentum barrier, or to study accretion on much smaller scales, but these will be left for future work. Thus in this work we still rely on a simple Bondi-like sub-grid model for gas accretion which, as detailed above, has significant limiting assumptions.

In addition to our novel refinement scheme, we implement concomitant changes to the algorithm by which black hole particles accrete and are advected, as well as the process by which mass is drained from the surrounding gas cells. The large gain in the mass and spatial resolution around black holes allows us to implement a more comprehensive black hole feedback model where mass, energy and momentum are imparted to the surrounding medium and where the resolved gas geometry dictates feedback geometry. We validate our implementation with a suite of simulation tests, before investigating the effect of these changes on models of isolated galaxies. While our refinement method allows us to track gas angular momentum much more accurately, for the purposes of this work we neglect the impact of gas angular momentum on the Bondi rate, which will be the main topic of our follow up paper. In addition, any such model will always be affected and potentially limited by its treatment of star formation and the structure of the interstellar medium (ISM). Ultimately to improve the accuracy of the modelling of black hole accretion it is clear that the subgrid models that govern star formation will also need to be improved.

The paper summary is as follows. In Section 2 we present our methodology and explain the details of our new implementation. In Section 3 we validate our implementation and choice of parameters on classical Bondi inflow solutions, while in Section 4 we present the results of our new refinement technique and black hole feedback on models of isolated, disc-dominated galaxies. Finally, in Section 5 we present our conclusions and discuss future work.

## 2 METHODOLOGY

### 2.1 Code

#### 2.1.1 Basic Setup

All simulations in this paper are carried out using the AREPO code (Springel 2010) which employs a moving mesh based on a quasi-Lagrangian finite volume technique. AREPO handles gravitational interactions using the TreePM

approach (Springel et al. 2005), and dark matter is modelled by a collisionless fluid of massive particles. In contrast to traditional adaptive mesh refinement (AMR) codes, which usually employ a Cartesian grid of cells that are then refined and de-refined according to some criteria, AREPO generates an unstructured mesh based on the Voronoi tessellation of a set of discrete points that cover the computational domain. These mesh-generating points are allowed to move freely with the local velocity of the flow, with some subdominant corrections to allow for mesh regularisation. In this way, AREPO retains many of the advantages of smoothed particle hydrodynamics (SPH) techniques such as Galilean invariance and resolution that naturally and continuously follows the fluid flow, as well as advantages of AMR methods such as better resolution of shocks, contact discontinuities and fluid instabilities (see e.g. Bauer & Springel 2012; Kereš et al. 2012; Sijacki et al. 2012; Torrey et al. 2012; Vogelsberger et al. 2012). In particular, for the purpose of this work, we exploit the code's ability to adaptively refine or de-refine the Voronoi mesh based on flexible criteria. Note that particle splitting techniques have been employed to allow for adaptive mass resolution in SPH codes (e.g. Kitsonas & Whitworth 2002; Martel et al. 2006; Mayer et al. 2015), while in AMR codes cells can be refined based on a number of predefined criteria, such as quasi- or super-Lagrangian refinements (e.g. Teyssier 2002; Chapon et al. 2013). Refinement in AREPO allows for smooth variations between regions of different mass resolution without imposing (relatively) sharp boundaries that may be prone to diffusion errors and numerical heating. The ability to de-refine in AREPO (that is, remove regions of high resolution) using a natural merging technique, is particularly important since refined particles may be moved large distances from a black hole by expulsive feedback.

For a subset of our simulations we adopt primordial gas cooling and a star formation sub-grid model as in Springel & Hernquist (2003). Gas cells above a density threshold of  $\rho_{\text{sfr}} = 0.18 \text{ cm}^{-3}$  stochastically form star particles, with a maximum formation time of  $t_{\text{sfr}} = 1.5 \text{ Gyrs}$ , which then only interact gravitationally with other particles in the simulation. Our model assumes that the ISM is in a self-regulated equilibrium state, representing the cumulative effect of unresolved thermal and turbulent processes, and that as such we can relate the average temperature as a function of density using an effective equation of state. To study the effect of colder gas present in the vicinity of black holes, we include metal line cooling in some simulations. Where present, we calculate this using the routine outlined in Vogelsberger et al. (2013) whereby cooling rates are calculated based upon the rates for a Solar abundance gas, scaled linearly with the total metallicity. As we are more interested in the range of the effect that the presence of cold gas can achieve we set the metallicity of all cells to be that of Solar composition gas. Note that as in Vogelsberger et al. (2013) metal line cooling is applied to the gas which is not in the multi-phase ISM.

#### 2.1.2 Refinement

AREPO applies well tested routines to regularize and (de-)refine the cells of the Voronoi mesh as appropriate. This results in the code being able to maintain the cells at a sim-

ilar target mass, as well as dynamically adapt to regions of higher density. Cells can also be flagged for refinement based on nearly arbitrary criteria, and this allows us to increase the spatial resolution over localized regions of the computational domain. Each cell selected is then split into two cells by the introduction of an additional mesh-generating point that is inserted at almost exactly the same location as that of the original cell, with conserved quantities, namely mass, energy and momentum, split between the new cells in a conservative manner<sup>†</sup>. The mesh-regularization techniques, which add a small additional corrective term to the velocity, in the direction of the centre of mass of the cell, mean that the two points become separated from each other over the course of a few timesteps. It is worth emphasizing that this is a key difference between AREPO and standard AMR codes: there is only ever a single mesh covering the simulation domain. In AREPO, by refinement, we mean the introduction of additional cells to increase the resolution over particular regions.

## 2.2 Novel refinement scheme around black holes

As described above, the criterion by which a cell is flagged for refinement can be almost arbitrary. We use this to our advantage when considering the problem at hand: improving the resolution and thus the estimation of the local properties of the gaseous fluid around black hole particles in our simulations. Here, we adopt a new strategy, by which cells are forced to have a radius that lies between two values, which increase linearly with distance from the nearest black hole.

Gas cells with cell radius  $R$  that are at a distance of  $d$  from a black hole are flagged for (de-)refinement if  $d < R_{\text{ref}}$  and if they lie outside of the range (see Figure 1)

$$\frac{d}{R_{\text{ref}}} \frac{(R_{\text{max}}^{\text{cell}} - R_{\text{min}}^{\text{cell}})}{c} + \frac{R_{\text{min}}^{\text{cell}}}{c} < R, \quad (3)$$

$$\frac{d}{R_{\text{ref}}} (R_{\text{max}}^{\text{cell}} - R_{\text{min}}^{\text{cell}}) + R_{\text{min}}^{\text{cell}} > R, \quad (4)$$

where  $c$  is a constant parameter that we set to 2. Our numerical experiments indicate that this value of  $c$  represents a balance between setting  $c$  too high, which would limit refinement or incur a large computational cost due to an overabundance of smaller cells, and setting  $c$  too low, which would mean that cells were forced to lie in a very strict range, leading to large computational cost as cells are constantly being refined and de-refined. In addition to this, we explicitly suppress stars from forming in the region  $d < R_{\text{ref}}$ . Allowing star particles to form from gas cells with a large mass spectrum increases the probability of collisions that can cause an unphysical increase in the kinetic or thermal energy of the smaller particle. By preventing our refined cells from forming stars we ensure there are no spurious  $N$ -body heating effects, which can affect the temperature of the gas local to the black hole, although there could still be some heating caused by dark matter particles moving through the central region of the galaxy. As we will see, the suppression does

<sup>†</sup> It is worth pointing out that the angular momentum conservation is not guaranteed in AREPO, but as shown in Pakmor et al. (2015) in the case of galaxy formation simulations it does not lead to any significant errors with respect to the schemes that exhibit second-order convergence in angular momentum conservation.

not have a significant impact on the overall star formation rate of the galaxy. In future work, we will develop more sophisticated representations of the ISM to better model star formation in the vicinity of black holes in order to make full use of our increased resolving power, but this is beyond the scope of this paper.

### 2.2.1 Choice of parameters

Within our refinement scheme, there are essentially three parameters to be defined: the volume over which we should refine which is set by  $R_{\text{ref}}$  as we assume spherical refinement regions, and the maximum  $R_{\text{max}}^{\text{cell}}$  and minimum  $R_{\text{min}}^{\text{cell}}$  radii, which define the spatial scale at which cells should be refined. Our strategy for choosing these parameters is motivated by several factors, namely

- (i) the refinement region should always contain at least a certain minimum mass of gas
- (ii) the accretion rate should be sufficiently resolved such that it converges to the results of higher resolution simulations
- (iii) the refinement scheme should not, inadvertently, de-refine cells as they enter the refinement radius
- (iv) computational overhead should be kept to a minimum
- (v) the Bondi radius is the physical scale that we want to resolve.

To guarantee the first of these, it makes sense to set  $R_{\text{ref}}$  to be a function of the black hole smoothing length,  $h_{\text{BH}}$ , which is defined as the radius of the sphere in which  $N_{\text{ngb}} \times m_{\text{target}}$  is present. Here  $N_{\text{ngb}}$  is the number of neighbouring gas cells which we set to at least  $32^{\ddagger}$ .  $m_{\text{target}}$  is the gas cell mass that AREPO maintains outside of the refinement region and which is typically equal to the gas cell mass at the beginning of the simulation. While values  $R_{\text{ref}} > h_{\text{BH}}$  give improved resolution over a larger volume, we find that this choice leads to no significant improvement in the accretion rate estimate over our simulations with  $R_{\text{ref}} = h_{\text{BH}}$ . This is because  $h_{\text{BH}}$  by definition contains a consistent mass which we find sufficient for the refinement scheme to be effective. Thus, all simulations in this paper use  $R_{\text{ref}} = h_{\text{BH}}$ , except where we explicitly state otherwise. It is worth pointing out that with our black hole refinement scheme we could in principle significantly reduce the black hole smoothing length (while keeping the refinement region larger) as the gas flow is much better resolved. However, for the purposes of this paper we keep the black hole smoothing length the same as in our non-refined simulations to allow for a more straightforward comparison between the two.

We find that by also setting  $R_{\text{max}}^{\text{cell}}$  to be a function of  $h_{\text{BH}}$  we are able to prevent the refinement scheme from merging cells inappropriately. After testing a range of different values we find that  $R_{\text{max}}^{\text{cell}} = 0.5 h_{\text{BH}}$  represents a good choice. We demonstrate this in Section 4, where we study the distribution of gas cell masses as a function of refinement parameters for isolated galaxy disc simulations.

<sup>‡</sup> Note that by default we increase  $N_{\text{ngb}}$  with resolution so as to ensure that the total enclosed mass within  $h_{\text{BH}}$  is constant.

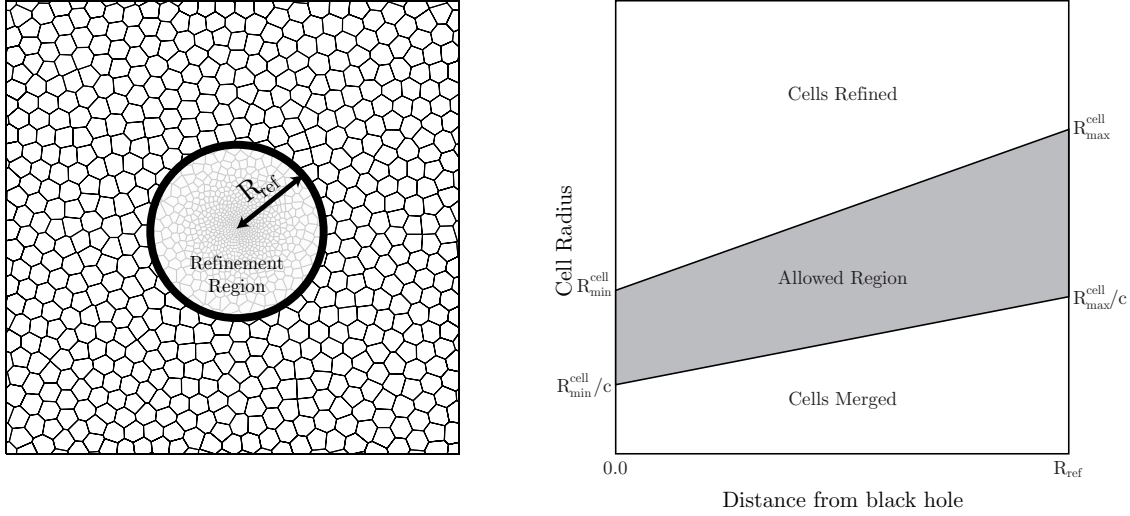


**Figure 1.** During normal code operation, cells are (de-)refined to keep their mass close to a pre-specified target value. Using our refinement scheme, however, we force cells within adaptively defined refinement radius,  $R_{\text{ref}}$ , (for a schematic representation, see the left-hand panel) to have a radius within the shaded zone indicated in the right-hand panel. If the cells lie outside of this shaded region, they are either refined (split into two) or de-refined (merged) as appropriate.

Finally, our goal of resolving scales of the order of the Bondi radius around the black hole motivates setting  $R_{\text{cell}}^{\text{min}}$  to be equal to  $r_{\text{B}}$  evaluated at each timestep when the black hole particle is active. Further to this, we impose a minimum cell mass to avoid excessive computational cost. The size of this is set by the maximum cell mass needed to resolve the Bondi radius. This is obviously dependent on the density of the gas close to the black hole, and so must be set experimentally. We find that a mass of  $m_{\text{min}} = 10^{-2} M_{\odot} \approx 10^{-7} m_{\text{target}}$ , valid for our specific simulations of isolated galaxies, is sufficient.

## 2.3 Black Hole Model

### 2.3.1 Black Hole Mass

Following previous studies (Di Matteo et al. 2005; Springel et al. 2005), we represent black holes using collisionless, massive sink particles. Our simulations maintain two separate black hole masses: the ‘sub-grid’ mass ( $M_{\text{BH,sub}}$ ) and the ‘dynamical’ mass ( $M_{\text{BH,dyn}}$ ). The sub-grid mass is the mass of the black hole for the purposes of the feedback algorithm: at each time step this mass increases by  $\dot{M}_{\text{BH}} dt$  and the resulting mass is used to calculate the subsequent accretion rate. The dynamical mass of the black hole particle is used in the calculation of the gravitational potential. This mass only increases via accreting mass from surrounding gas cells or by merging with other black hole particles.

The need for two masses is driven by the problems of resolving the black hole properly. Gas cells surrounding the black hole frequently have masses that are the same order of magnitude as, or even larger than, the black hole itself. Allowing the black hole to accrete neighbouring gas cells directly would therefore be unphysical. Ideally, the increase in the sub-grid mass  $M_{\text{BH,sub}}$  should be paralleled by increases

in the dynamical mass  $M_{\text{BH,dyn}}$  so that the code maintains  $M_{\text{BH,dyn}} = M_{\text{BH,sub}}$  as closely as possible, which in practice is true once the sub-grid mass exceeds the gas cell mass.

The possibly large masses of the gas cells in our simulations relative to the black hole particle mass (especially in the case of the initial black hole seed) mean that the black hole is prone to being ejected by unphysical two-body encounters. We note that this is a problem that is present in all simulations with comparable dark matter/gas mass and black hole seed mass. Other studies have forced the black hole position to track the potential minimum of their host halo. We find, however, that once we resolve the flow around the black hole this leads to unacceptable movement of the black hole. In this paper, we instead allow the black hole particle to have a relatively large dynamical mass. This mass is set to be large enough such that the black hole is subject to sufficient dynamical friction that it remains in the centre, but small enough such that we do not introduce large changes to the central potential. We find that  $M_{\text{BH,dyn}} = 200 \times M_{\text{DM}}$  is the sufficient mass required to maintain the black holes particles in the correct position. Note also that, due to our super-Lagrangian refinement, the typical gas cell mass in the vicinity of black holes is much smaller than is the case without the refinement, which further minimizes artificial black hole displacements.

### 2.3.2 Accretion Rate

Following Springel et al. (2005), we take as our fiducial model a Bondi-Hoyle-like prescription to estimate the accretion on to the black hole

$$\dot{M}_{\text{B}} = \frac{4\pi\alpha G^2 M_{\text{BH}}^2 \rho_{\infty}}{c_{\infty}^3}, \quad (5)$$

where  $M_{\text{BH}}$  is the mass of the black hole,  $\rho_\infty$  is the gas density at infinity and  $c_\infty$  is the sound speed at infinity. The traditional Bondi-Hoyle-Lyttleton rate also includes the relative velocity of the black hole. For simplicity, we do not include this here. Here,  $\alpha = 100$  is a dimensionless parameter that we use to account for the unresolved cold and hot ISM phases (for further discussion see Sijacki et al. 2011). In addition, in all simulations we limit the accretion rate to the Eddington limit

$$\dot{M}_{\text{Edd}} \equiv \frac{4\pi G M_{\text{BH}} m_{\text{p}}}{\epsilon_{\text{r}} \sigma_{\text{T}} c}, \quad (6)$$

where  $\sigma_{\text{T}}$  is the Thomson cross-section,  $m_{\text{p}}$  is the mass of a proton and  $\epsilon_{\text{r}} = 0.1$  is the radiative efficiency. For non-spherically symmetric accretion, it is possible for accretion to exceed the Eddington limit, for example, if energy is transported away by a collimated outflow (Kurosawa & Proga 2009; Jiang et al. 2014). The extent to which AGN accrete in super-Eddington regimes is as yet unclear, but it is not something that we consider in this paper.

In calculating the fluid properties in the locality of the black hole, we must average over the central volume weighted by the mass of the gas cells and (optionally) by some kernel function. In SPH codes this is handled naturally, as the value of each field centred on the black hole is by default just the SPH kernel weighted sum evaluated at the black hole's position. Here, we adopt a similar technique with top-hat kernel and simply calculate the fluid properties as a mass weighted sum over the black hole smoothing length. We choose this top-hat approach over other alternatives (such as a cubic spline kernel) as we do not wish to overweight the innermost gas cells in our calculations given that we are resolving the physical scales relevant for Bondi accretion.

### 2.3.3 Cell Draining

When the sub-grid mass increases, we must drain mass from surrounding gas cells to ensure mass conservation. To accomplish this we adopt a model similar to that of the previous simulations of Vogelsberger et al. (2013), in which up to 90% of gas is drained from the primary cell of the black hole particle. Here, however, our refinement scheme forces cells to become progressively smaller the closer they are to the black hole. Limiting this process to a single cell means that there is often not enough mass available - the black hole cannot keep up and gas builds up causing the accretion rate to rise. We avoid this problem by allowing mass to be drained from multiple cells surrounding the black hole. We do this by allowing the sink particle to drain up to 90% of a cell's mass in a manner weighted by the mass of the cell. At each time step, the black hole attempts to drain  $\Delta M = (1 - \epsilon_{\text{r}}) \dot{M}_{\text{BH}} \Delta t$  from the cells within its smoothing length. A cell of mass  $m$  is drained of  $\Delta m = \Delta M \frac{m}{m_{\text{tot}}}$ , where  $m_{\text{tot}}$  is the total mass of gas cells within the black hole smoothing length.

### 2.3.4 Feedback

Here we adopt two different mechanisms of injecting feedback. In each, the AGN luminosity is set to be a fraction  $\epsilon_{\text{r}}$  of the rest mass energy available from accreting material.

In the first case, feedback is implemented by coupling a

fraction  $\epsilon_{\text{f}}$  of the luminosity thermally and isotropically to the surrounding gas, so that

$$\Delta E_{\text{feed}} = \epsilon_{\text{f}} \epsilon_{\text{r}} \Delta M_{\text{BH}} c^2; \quad (7)$$

$\epsilon_{\text{f}} = 0.05$  here represents the feedback efficiency, which we set to reproduce the normalization of the locally inferred  $M_{\text{BH}} - \sigma$  relation (Di Matteo et al. 2005; Sijacki et al. 2007). The energy is distributed over all cells within the smoothing length of the black hole, weighted according to a simple cubic spline kernel, as given by Monaghan & Lattanzio (1985). Note that this is different to the top-hat kernel that we use for estimation of the fluid parameters for the Bondi rate. There is no particular reason why these two kernel weightings should be the same in grid based codes. In this case, we are motivated by wanting to model energy released in the immediate vicinity of the black hole, in contrast to the estimation of fluid parameters at a larger distance from the black hole (i.e.  $\rho_\infty, c_\infty$ ) as with the accretion rate calculation.

In the second case, we inject a total momentum of  $L/c$  into the cells surrounding the black hole. In the simplest case we inject the momentum isotropically as well (see also Costa et al. 2014). Similar to above, each cell within the smoothing length of the black hole receives a kick to its momentum, weighted according to the cubic spline kernel, in the radial direction away from the black hole.

### 2.3.5 Non isotropic accretion and feedback

The traditional approach of estimating the fluid parameters and injecting the feedback energy via a simple, isotropic algorithm fails to make use of the increased resolving power enabled by our super-Lagrangian refinement technique. To overcome this, in this paper we explore the effects of a non-isotropic scheme on our black hole model.

In certain physical configurations (e.g. efficient cooling of gas with significant angular momentum) accreting material should consist of a cold, dense disc component as opposed to the hot, spherically symmetric gas. We attempt to model this by defining the cold component of the gas within the smoothing length of the black hole as that with a temperature below  $T_{\text{cold}}$ . Whenever this cold component makes up a fraction of at least  $f_{\text{cold}}$  of the mass of the gas within the smoothing length, we enter a non isotropic mode of accretion. Here we estimate the fluid parameters (i.e.  $c_\infty, \rho_\infty$ ) only from the cold component, otherwise we proceed as before in taking all gas within the smoothing length<sup>§</sup>. For consistency, when adopting this method we also limit the draining of mass from the gas cells surrounding the black hole to those cells in the disc component. There are clearly more sophisticated ways of accurately isolating the cold component of the gas, but we wish to keep our method as simple as possible and to make as few assumptions as possible, since this will allow us to apply it to a cosmological context, where gas can have a very complex morphology.

We also adapt our feedback algorithms to implement a

<sup>§</sup> Note that with this model we only explore how inflowing gas geometry affects our accretion model rather than attempting to self-consistently track the black hole accretion disc, which occurs below our resolvable scale.

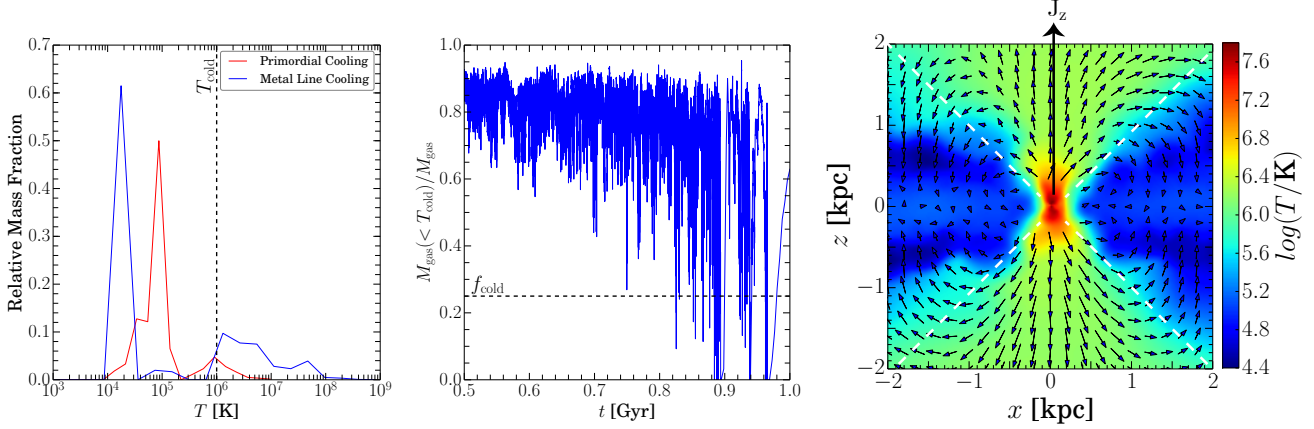


**Figure 2.** In the left-hand panel, we show the temperature distribution of the gas within the black hole smoothing length, which is typically around 1 kpc. Here we show the distribution for our normal isotropic thermal feedback model (red), and that for a similar simulation with metal line cooling (blue). The majority of the gas is within a clearly distinguished cold component at around  $10^5$  K (red) and  $10^4$  K (blue). The feedback heated gas is clustered around  $10^6$  K. In our bipolar model we measure the fraction of gas that is present in the cold component, which can be seen in the middle panel, and if the fraction is larger than  $f_{\text{cold}} = 0.25$  we estimate the properties of the accreting gas solely from that same cold component. In the right-hand panel we show gas temperature map using the bipolar feedback model. Overplotted arrows indicate the direction and relative velocity of the gas, and we also show the feedback cone (dashed white lines) and angular momentum axis of the accreting gas,  $\mathbf{J}_z$ .

non isotropic scheme. Here, we are motivated by unresolved dynamics that lead to observed bipolar outflows from AGN (Rupke & Veilleux 2011; Maiolino et al. 2012). These may be driven by magnetic fields close to the black hole that we do not attempt to model in these simulations, or could be hydrodynamically driven on larger scales. Instead, we allow for their effects by implementing both the thermal and momentum schemes detailed above, limiting them to a double cone of opening angle  $\theta_{\text{out}}$  with axis parallel to the axis of the angular momentum vector of the gas around the black hole which is an assumption of our model (see also Ostriker et al. 2010; Choi et al. 2014). In addition, we also allow the feedback to entrain mass in the outflow. We specify an efficiency parameter  $\epsilon_{\text{out}}$  which represents the fraction of accreting gas that is swept up into the outflow. We inject the resulting mass into gas cells within the double cone, weighting by the cubic spline kernel, in an exact reverse of our draining procedure.

### 2.3.6 Parameter choices

We now describe how we set values for the free parameters,  $T_{\text{cold}}$ ,  $f_{\text{cold}}$ ,  $\epsilon_{\text{out}}$  and  $\theta_{\text{out}}$  that define how black holes accrete from the cold component of the gas. Left-hand panel of Figure 2 shows an example of a typical distribution of the gas temperature for our isotropic thermal feedback scheme, as well as for a similar simulation but with additional metal line cooling. A clearly distinct cold component can be seen around  $10^5$  K in the standard feedback model and at around  $10^4$  K in the case of metal line cooling. This is typical of the values that we see across our simulations (other than when the gas of the galaxy is exhausted at late times), and motivates using a temperature  $T_{\text{cold}} = 10^6$  K. Increasing this temperature to values above  $10^7$  K recovers the results of our isotropic simulations.

Similarly, we set  $f_{\text{cold}}$ , the fraction of the mass of the gas that needs to be below the critical temperature in order for

us to estimate the accretion parameters from the cold component, to 0.25. We have investigated different choices of this parameter, but for values  $< 0.4$  we find that the results do not change noticeably. This can be explained by the middle panel of Figure 2, which shows the typical evolution of the fraction of cold gas prior to the destruction of the central region of the disc (which happens at late times due to build up of feedback energy). Here we see that until  $t \sim 0.8$  Gyr, the mass of accreting gas present is well above our threshold, rendering the simulation insensitive to small changes in this value. At later times, as the cumulative feedback energy becomes significant, the cold fraction drops until it eventually reaches the range when we switch to isotropic feedback. However, when this happens, the rate of change of the cold fraction is very fast - beyond a certain point, the cold disc component is quickly overcome. As such, changes in  $f_{\text{cold}}$  result in the model switching to isotropic feedback at nearly identical times.

We set  $\theta_{\text{out}}$ , the opening angle of the bipolar outflow, to be  $\pi/4$ . In test simulations, we find that for a broad range of opening angles, the accretion rate is consistent. This is perhaps unsurprising, since in this case we estimate the fluid parameters from the cold component and not from the hot outflow, and the majority of the accreting gas is centred in the plane perpendicular to the angular momentum axis. We set the efficiency of the entrainment of the gas into the outflow to  $\epsilon_{\text{out}} = 0.5$ . This in principle may be much higher - Choi et al. (2014) for example, find that mass and energy conservation (based upon an outflowing wind velocity of  $10000 \text{ km s}^{-1}$  and the same feedback efficiency used here) imply that 90% of the in-falling gas will be expelled in a wind. Our choice thus represents a more conservative value; a full study of the impact of this parameter will follow in a future paper. Right-hand panel of Figure 2 shows the result of this bipolar model in practice. Here we plot a temperature map through the  $x-z$  plane of the simulation, with the black hole centred at the origin. The imprint of the bipolar

outflow is visible in the centre, with the gas strongly heated to almost  $10^8\text{K}$ .

We also check that our measurement of the gas angular momentum (and as such the direction along which we inject feedback) is robust. This is especially important as any fluctuation in the axis of the feedback cone could lead to the disc being destroyed prematurely. We confirm that in our simulations of isolated galaxies, for which the net angular momentum axis should align with the  $z$  axis, whilst the cold disc is present, our estimated angular momentum for the surrounding gas is consistently aligned with the  $z$  axis. We further verify that maintaining a fixed angular momentum vector along this axis does not change the results.

### 2.3.7 Duty cycle

In addition to injecting feedback at each time step, we also investigate the effects of allowing the feedback energy to build up over a time-scale  $t_{\text{cycle}}$ . Note that here, the time-scale defined is the time between feedback events, not the length of the burst. After this time has elapsed, the accreted energy is released in a single feedback event, and the cycle repeats. This mimics the observed characteristics of AGN duty cycles, but the time-scales themselves are poorly constrained. For the purposes of this paper, we are interested in the effects on the sound speed of the gas, since this will affect black hole accretion rate. A full parameter study is beyond the scope of this paper - here we set  $t_{\text{cycle}}$  to  $10^8\text{yr}$  as it was found that this was long enough to have a substantial impact of the gas properties, but short enough to allow a significant number of accretion events across the full time span of our simulations.

## 3 RESULTS: BONDI INFLOWS

### 3.1 Initial Conditions

As a first test of our refinement technique we verify it's ability to improve the resolution of the fluid flow in the region around the black hole. For this purpose we carry out a series of simulations, where the black hole is surrounded by a spherically symmetric gas distribution and where there is no net bulk relative velocity between the gas and the black hole. By considering these idealized initial conditions we can directly compare our measure of gas accretion on to the central object with the theoretical Bondi rate, and examine how this changes when our refinement scheme is used.

We generate initial conditions based on the theoretical density and velocity profiles of spherically symmetric accretion on to a point mass (Bondi 1952b). The gas is characterized by its properties at infinity, where it is at rest and has a uniform density  $\rho_\infty$  and pressure  $p_\infty$ . Conservation of mass gives the equation

$$\dot{M} = -4\pi r^2 \rho v, \quad (8)$$

where  $\dot{M}$  is the constant mass accretion rate. Bernoulli's equation then gives

$$\frac{1}{2}v^2 + \left(\frac{\gamma}{\gamma-1}\right) \frac{p_\infty}{\rho_\infty} \left[ \left(\frac{\rho}{\rho_\infty}\right)^{\gamma-1} - 1 \right] = \frac{GM_{\text{BH}}}{r}, \quad (9)$$

where we have assumed a Newtonian gravitational potential for the central supermassive black hole, as well as a polytropic equation of state such that  $p/p_\infty = (\rho/\rho_\infty)^\gamma$ , for  $1 \leq \gamma \leq 5/3$ .

The accretion rate is then given by

$$\dot{M} = \frac{4\pi\lambda G^2 M_{\text{BH}}^2 \rho_\infty}{c_\infty^3}, \quad (10)$$

where  $\lambda$  is a non-dimensional parameter equal to (Bondi 1952b)

$$\lambda = \left(\frac{1}{2}\right)^{\frac{\gamma+1}{2(\gamma-1)}} \left(\frac{5-3\gamma}{4}\right)^{\frac{3\gamma-5}{2(\gamma-1)}}. \quad (11)$$

We solve Equations 8 and 9 for the two unknowns,  $\rho(r)$  and  $v(r)$ , which we hereafter refer to  $\rho_{\text{B}}(r)$  and  $v_{\text{B}}(r)$ , respectively. We then use these as the basis for generating our initial conditions.

We use a near identical setup to that of Barai et al. (2011): we generate a spherical distribution of gas surrounding a central supermassive black hole with mass  $M_{\text{BH}} = 10^8 M_\odot$ . We distribute the gas by randomly sampling from the cumulative mass distribution given by  $\rho_{\text{B}}(r)$ , and then by setting the appropriate radial velocity  $v_{\text{B}}(r)$ . The gas is distributed between an inner radius  $r_{\text{in}}$  and an outer radius  $r_{\text{out}}$  and we set  $T_\infty = 10^7\text{K}$  and  $\rho_\infty = 10^{-19}\text{g cm}^{-3}$ . We set  $\gamma = 1.01$  which, coupled with a value of  $r_{\text{in}} = 0.1\text{pc}$  and  $r_{\text{out}} > 10\text{pc}$  means that both  $r_{\text{B}} = 3.0\text{pc}$  and  $r_{\text{sonic}} = 1.5\text{pc}$  (the point at which the in-falling gas becomes supersonic) lie well within our simulation domain.

### 3.2 Numerical setup

We make some minor adjustments to our code in order to enforce the boundary conditions of the theoretical setup. We ensure that gas cells situated at a distance of more than  $r_{\text{out}}$  from the centre of the simulation have the parameters of the gas at infinity - i.e.  $T_\infty$ ,  $\rho_\infty$ ,  $p_\infty$  - and that they are stationary. In principle this means there is a small discontinuity in the density distribution at  $t = 0$  that decreases with larger values of  $r_{\text{out}}$ . We examine the effects of this in the section below. In these simulations, we replace our usual estimate of the accretion based on the large scale fluid properties with a routine that swallows individual gas cells. In the centre of the simulation domain, we use a simple sink particle routine to remove gas cells from the region closest to the black hole. Here, we remove all cells that have both mesh generating points and estimated semi-major axes (of their orbit around the black hole) within  $r_{\text{in}}$ . We do, however, keep the mass of the central black hole fixed to maintain a constant theoretical accretion rate with time. This does not substantially affect the results, as the total accreted mass throughout our simulations represents at most about 5% of  $M_{\text{BH}}$ . We sum the mass of all cells removed at the inner radius and take this as our estimate of the accretion rate. For completeness, we also calculate the total mass of cells within the Bondi radius. We check that this remains constant throughout the simulation, indicating that (as expected) the flux across the Bondi radius is the same as that across the inner radius and that for sufficiently small radii, the choice of  $r_{\text{in}}$  does not affect our results.

We run a suite of simulations (see Table 1), varying both the number of gas cells  $N_{\text{gas}}$  and the outer truncation



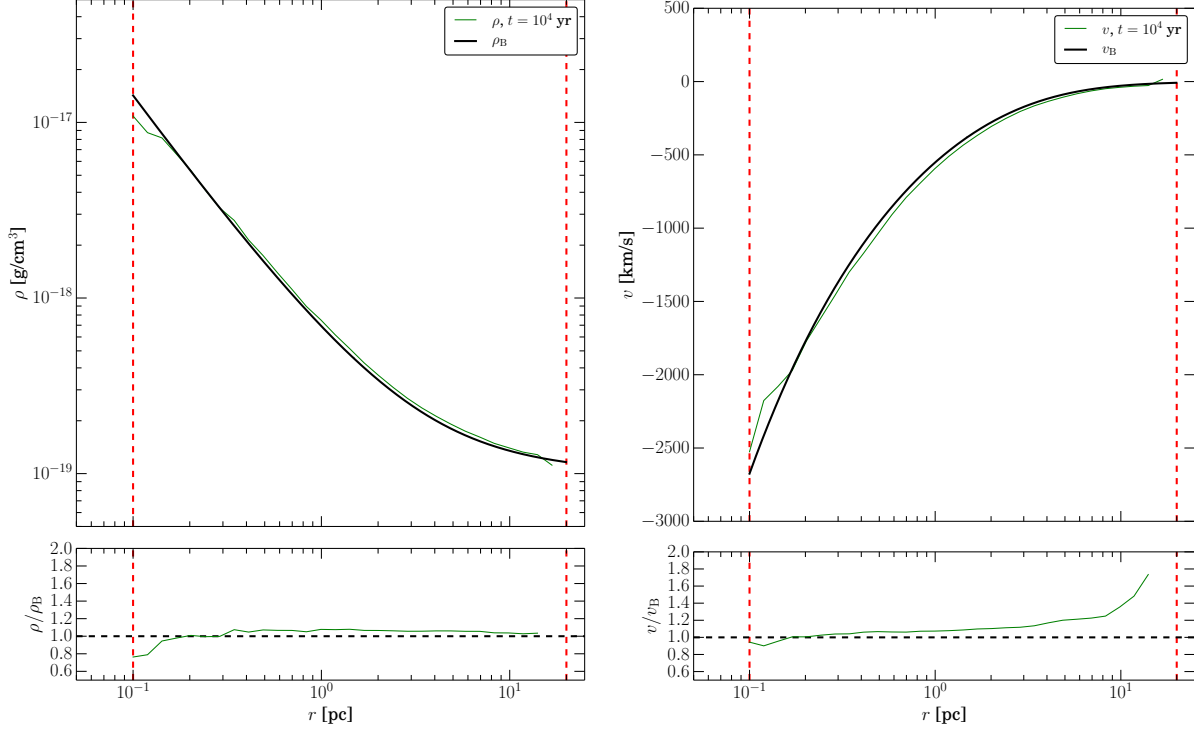


**Figure 3.** Radial profiles of gas density (left-hand panel) and gas velocity (right-hand panel). The black curves denote the analytical Bondi solution while the green curves are our simulation results at  $t = 10^4$  yrs for our simulation without refinement, with  $64^3$  initial resolution elements. Red, vertical dotted lines indicate  $r_{\text{in}} = 0.1$  pc and  $r_{\text{out}} = 20$  pc. In the lower panel, we show the ratio of the analytic profile with the measured one. Small departures from the analytical solution at radii close to  $r_{\text{in}}$  occur due to the inner boundary condition imposed there, but note that their effect is negligible given that the Bondi radius is located at  $r_B = 3.0$  pc.

| Name               | $N_{\text{gas}}$ | $r_{\text{out}}$ (pc) | Refinement | $R_{\text{ref}}$ (pc) | $R_{\text{cell}}^{\text{min}}$ (pc) | $R_{\text{cell}}^{\text{max}}$ (pc) | CPU time (h) |
|--------------------|------------------|-----------------------|------------|-----------------------|-------------------------------------|-------------------------------------|--------------|
| NoRef $16^3$       | $16^3$           | 20                    | No         | -                     | -                                   | -                                   | 4.4          |
| NoRef $32^3$       | $32^3$           | 20                    | No         | -                     | -                                   | -                                   | 12.3         |
| NoRef $64^3$ 10 pc | $64^3$           | 10                    | No         | -                     | -                                   | -                                   | 102.4        |
| NoRef $64^3$ 15 pc | $64^3$           | 15                    | No         | -                     | -                                   | -                                   | 91.3         |
| NoRef $64^3$       | $64^3$           | 20                    | No         | -                     | -                                   | -                                   | 75.2         |
| Ref $16^3$         | $16^3$           | 20                    | Yes        | 1.0                   | 0.01                                | 1                                   | 5.0          |
| Ref $32^3$         | $32^3$           | 20                    | Yes        | 1.0                   | 0.01                                | 1                                   | 14.4         |
| RefAggr $32^3$     | $32^3$           | 20                    | Yes        | 1.0                   | 0.001                               | 0.5                                 | 54.6         |

**Table 1.** Simulation details of Bondi inflow models. First column lists the name of simulations performed, second column indicates the initial number of gas cells used, while third column gives the outer radius of the simulation domain beyond which gas conditions at infinity are imposed. In the fourth column we indicate if the super-Lagrangian refinement scheme is used or not, and for the subset of simulation with refinement on, we list the refinement parameters, namely  $R_{\text{ref}}$ ,  $R_{\text{cell}}^{\text{min}}$  and  $R_{\text{cell}}^{\text{max}}$  in columns five, six and seven, respectively. Finally, in column eight we show the total CPU hours used by  $t = 6 \times 10^4$  yrs.

radius  $r_{\text{out}}$  for simulations with and without refinement. For simulations in which the refinement scheme is active, we also examine the effects of more aggressive refinement (by changing the refinement parameters  $R_{\text{min}}^{\text{cell}}$  and  $R_{\text{max}}^{\text{cell}}$ ).

In Figure 3 we plot the radial profiles of gas density (left-hand panel) and gas velocity (right-hand panel). Black curves denote analytical Bondi solution while green curves are our simulation results at  $t = 10^4$  yrs (NoRef  $64^3$ ). The simulation results agree very well with the analytical profiles over the whole simulated timespan and over the simulated spatial domain. We note that there are small departures from the analytical solutions close to the inner,  $r_{\text{in}}$ , and outer,  $r_{\text{out}}$ , boundary conditions. Their effect is however very small (as we have explicitly checked by varying the values of  $r_{\text{in}}$  and  $r_{\text{out}}$ ) given that the Bondi radius is located at  $r_B = 3.0$  pc.

ures from the analytical solutions close to the inner,  $r_{\text{in}}$ , and outer,  $r_{\text{out}}$ , boundary conditions. Their effect is however very small (as we have explicitly checked by varying the values of  $r_{\text{in}}$  and  $r_{\text{out}}$ ) given that the Bondi radius is located at  $r_B = 3.0$  pc.

### 3.3 Impact of resolution and refinement method

In the left-hand panel of Figure 4 we show the results of our simulations without refinement for three different resolutions:  $16^3$ ,  $32^3$  and  $64^3$  initial gas cells. We also plot the

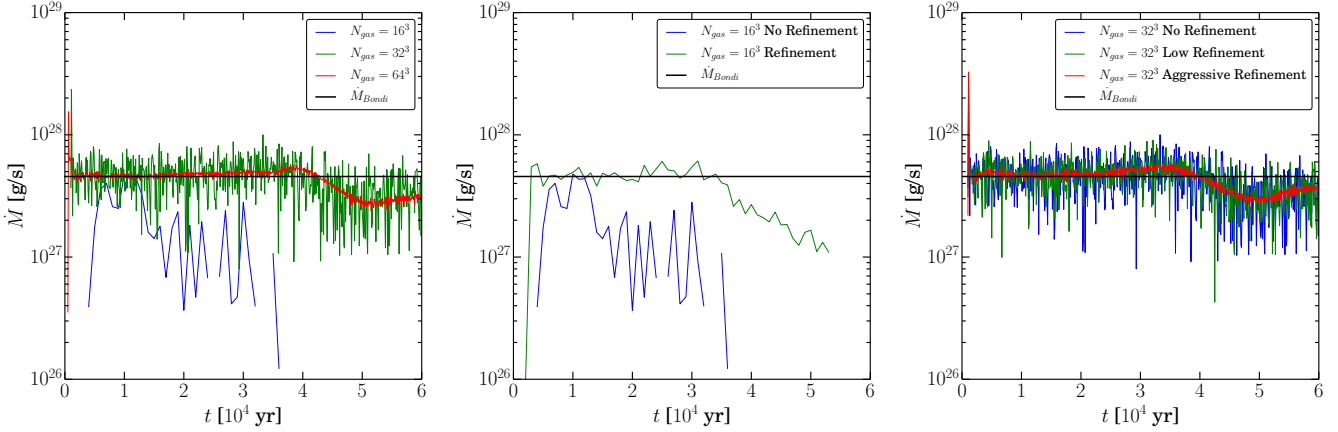


**Figure 4.** Mass inflow rate across  $R = 0.1$  pc averaged over a fixed size timestep  $dt$  for simulations with  $N_{\text{gas}} = 16^3, 32^3$  and  $64^3$  gas cells ( $dt = 1000$  yr for  $N_{\text{gas}} = 16^3$ ,  $dt = 100$  yrs otherwise). The analytic solution is indicated by the horizontal solid black line. Left-hand panel: results without our super-Lagrangian refinement for three different resolutions as shown on the legend. Central panel: comparison of the results without and with black hole refinement at a fixed resolution of  $N_{\text{gas}} = 16^3$ . Right-hand panel: no, moderate and aggressive refinement at a fixed resolution of  $N_{\text{gas}} = 32^3$ . Note that the discrepancy between the analytical prediction and simulation results for  $t \gtrsim 4 \times 10^4$  yr is entirely due to the location of the outer boundary condition (i.e. the size of the simulated region; see text for more details).

theoretical accretion rate  $\dot{M}_B$  denoted with the horizontal black line. For the highest resolution case we find excellent agreement with the theoretical rate, with the exception for  $t \gtrsim 4 \times 10^4$  yrs. This coincides with the sound travel time from our truncation radius to the centre of the simulation domain, and this is the effect of the small discontinuity in our initial conditions. We confirm this by checking the accretion rate for simulations with successively smaller values of  $r_{\text{out}}$  and find a linear relation between truncation radius and the feature seen here. The simulations are otherwise identical, and after the wave has propagated the simulations return to the theoretical rate.

For the medium resolution case, we see that there is still good agreement with the theoretical picture, but with heightened stochasticity due to the Poisson noise. By the time we get to our lowest resolution simulation, however, the resolution is too coarse to correctly model the Bondi inflow and we do not match  $\dot{M}_B$ .

The central panel of Figure 4 shows an identical setup with  $16^3$  initial gas cells with and without our refinement technique. Here we see that the simulation with super-Lagrangian refinement does a much better job - even with the low resolution initial conditions we are able to reproduce the theoretical Bondi accretion rate and the total CPU time used lies in between the costs for the  $16^3$  and  $32^3$  runs without refinement.

Furthermore, right-hand panel of Figure 4 shows how changing the aggression of the refinement parameters affects the simulated accretion rate. Here we show the medium resolution case with initial  $32^3$  gas cells. With moderate refinement, the stochasticity of the cell flux over the inner radius is reduced, but only slightly. For more aggressive parameters this is dramatically reduced and we are able to reproduce an accretion rate that is nearly identical to the run with eight times the number of cells at somewhat lower CPU cost.

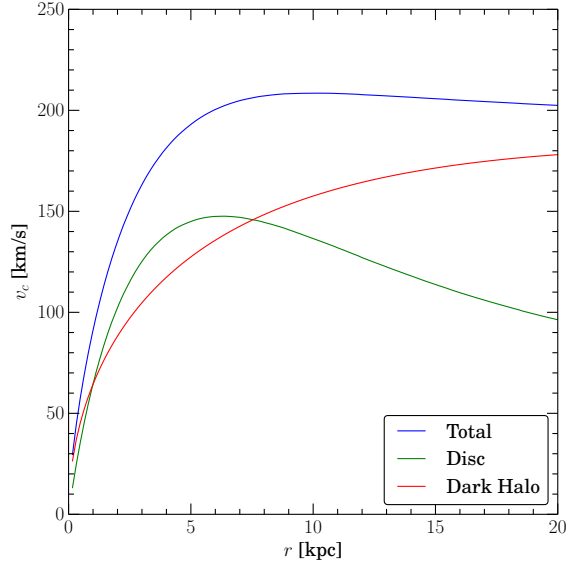


**Figure 5.** Rotation curves for our model galaxies, with parameters as detailed in Table 2. The red line shows the circular velocity as a function of radius for the dark matter halo, whilst the green line shows the same for the disc component. The blue line shows the total rotation curve.

## 4 RESULTS: ISOLATED DISC GALAXY SIMULATIONS

### 4.1 Initial conditions

We investigate the effects of our new refinement scheme using simple models of isolated galaxies, as described by Springel et al. (2005). Each galaxy consists of a dark matter

| Parameter        | Value                           | Description                                     |
|------------------|---------------------------------|-------------------------------------------------|
| $c$              | 9.0                             | Halo concentration                              |
| $v_{200}$        | $160 \text{ km s}^{-1}$         | Virial velocity                                 |
| $M_{200}$        | $9.52 \times 10^{11} M_{\odot}$ | Virial mass                                     |
| $m_d$            | 0.041                           | Disc mass fraction                              |
| $m_b$            | 0                               | Bulge mass fraction                             |
| $h$              | 2.74 kpc                        | Disc scalelength                                |
| $z_0$            | 0.2 $h$                         | Disc scaleheight                                |
| $\lambda$        | 0.033                           | Spin parameter                                  |
| $m_{\text{BH}}$  | $10^5 - 10^6 M_{\odot}$         | Black hole seed mass                            |
| $f_{\text{gas}}$ | 0.1                             | Gas mass fraction of the disc                   |
| $J_d$            | 0.041                           | $m_d \times$ total angular momentum of the halo |

**Table 2.** Parameter choices for the isolated galaxy models.

halo with a Hernquist (1990) density profile

$$\rho_{\text{dm}} = \frac{M_{\text{dm}} a}{2\pi r(r+a)^3}, \quad (12)$$

where  $M_{\text{dm}}$  is the total dark matter mass and  $a$  is a scaling parameter. This profile has the advantage that for inner radii it is similar to the Navarro, Frenk and White (Navarro et al. 1996, NFW) model but has a finite mass. The two can be related by choosing

$$a = r_s \sqrt{2(\ln(1+c) - c/(1+c))}, \quad (13)$$

where  $c = r_{200}/r_s$  is the concentration index of the NFW halo, and  $r_s$  is the scale radius. Both gaseous and stellar discs are modelled using an exponential surface density profile:

$$\Sigma_{\text{gas}}(r) = \frac{M_{\text{gas}}}{2\pi h^2} e^{-r/h}, \quad (14)$$

$$\Sigma_{\star}(r) = \frac{M_{\star}}{2\pi h^2} e^{-r/h}, \quad (15)$$

where  $h$  is the scalelength of the disc,  $M_{\text{gas}}$  is the total initial gas mass and  $M_{\star}$  is the total initial stellar mass. By assuming that the disc is centrifugally supported and that it is negligibly thin compared to its scalelength,  $h$ , its angular momentum can be expressed by

$$J_d = M_d \int_0^{\infty} v_c(R) \left(\frac{R}{h}\right)^2 e^{-\frac{R}{h}} dR, \quad (16)$$

where  $M_d$  is the total mass in the disc,  $R$  is the cylindrical radius and  $v_c$  is the circular velocity.

The vertical mass distribution of the stellar disc is given the profile of an isothermal sheet, resulting in a three dimensional stellar density distribution of

$$\rho_{\star}(R, z) = \frac{M_{\star}}{4\pi z_0 h^2} \text{sech}^2\left(\frac{z}{z_0}\right) e^{-\frac{R}{h}}, \quad (17)$$

where  $z_0$  determines an effective temperature of the disc. The velocity dispersion is then set to self-consistently maintain this scaleheight in the full 3D potential of the model.

The gaseous disc is governed by hydrostatic equilibrium, whereby the azimuthal velocity is set to ensure balance between the inward gravitational and the outward combination of centrifugal and pressure support

$$v_{\phi, \text{gas}}^2 = R \left( \frac{\partial \Phi}{\partial R} + \frac{1}{\rho_{\text{gas}}} \frac{\partial P}{\partial R} \right), \quad (18)$$

with the remaining velocity components  $v_R = v_z = 0$ . An

initial distribution is found, which is used as the basis for an iterative method which produces a self-consistent gas distribution and potential. Table 2 shows our parameter choices, which are chosen to represent a simplified typical Milky Way-like disc galaxy, with the rotation curves for different components shown in Figure 5. Table 3 lists the full suite of isolated disc galaxy simulations that we have performed.

## 4.2 Validation of Implementation

In Figure 6 we validate our super-Lagrangian refinement scheme on the models of isolated disc galaxies which are evolved for 10 Gyrs in total. In the left-hand panel we plot the distribution of cell masses normalized to the target gas mass. With the standard de-/refinement of gas cells present in AREPO the cell mass distribution peaks around the target value and extends within a factor of  $\sim 2$  from the peak value (blue curve). With our super-Lagrangian refinement around black holes the distribution of cell masses at the high mass end (beyond the target value) is essentially identical. This validates our choice of  $R_{\text{cell}}^{\text{max}} = 0.5 h_{\text{BH}}$  and explicitly demonstrates that we are not unnecessarily de-/refining the cells once they enter or leave the black hole refinement region. The distribution of cell masses below the target value is however markedly different. This is caused by the cells within our super-Lagrangian refinement region where we extend the dynamical range in mass by more than six orders of magnitude. Note that the low mass cutoff is due to the imposed minimum cell mass, as denoted with the vertical dashed line.

In the central panel of Figure 6 we show the mass distribution of stellar particles with and without the refinement scheme. The two show very good agreement, indicating that our refinement scheme is not introducing a broad range of stellar particle masses, which could lead to unwanted  $N$ -body heating. Furthermore, the right-hand panel of Figure 6 demonstrates that the star formation rate evolution is not artificially affected in simulations with super-Lagrangian refinement where we do not allow gas cells in the refinement region to be star forming. In fact the star formation rates are broadly the same regardless of the refinement scheme being used or not, with the slightly larger star formation rates at late times in the refinement case caused by the slightly lower rate of accretion on to the central black hole.

Figure 7 shows more explicitly how our refinement

| Name                          | N               | Refinement | Accretion                                       | Feedback   | $m_{\text{target}}$ ( $M_{\odot}$ ) | $\epsilon_{\text{DM}}$ (kpc) | $\epsilon_{\text{gas}}$ (kpc) | Cooling    |
|-------------------------------|-----------------|------------|-------------------------------------------------|------------|-------------------------------------|------------------------------|-------------------------------|------------|
| NoRef 10 <sup>5</sup>         | 10 <sup>5</sup> | None       | Default Bondi                                   | Thermal    | $2.0 \times 10^5$                   | 2.0                          | 0.15                          | Primordial |
| NoRef 10 <sup>6</sup>         | 10 <sup>6</sup> | None       | Default Bondi                                   | Thermal    | $2.0 \times 10^4$                   | 0.93                         | 0.07                          | Primordial |
| NoRef 10 <sup>7</sup>         | 10 <sup>7</sup> | None       | Default Bondi                                   | Thermal    | $2.0 \times 10^3$                   | 0.43                         | 0.032                         | Primordial |
| RefNorm 10 <sup>5</sup>       | 10 <sup>5</sup> | Yes        | Default Bondi                                   | Thermal    | $2.0 \times 10^5$                   | 2.0                          | 0.15                          | Primordial |
| RefNorm 10 <sup>6</sup>       | 10 <sup>6</sup> | Yes        | Default Bondi                                   | Thermal    | $2.0 \times 10^4$                   | 0.93                         | 0.07                          | Primordial |
| RefNorm 10 <sup>7</sup>       | 10 <sup>7</sup> | Yes        | Default Bondi                                   | Thermal    | $2.0 \times 10^3$                   | 0.43                         | 0.032                         | Primordial |
| RefNorm 10 <sup>5</sup>       | 10 <sup>5</sup> | Yes        | Default Bondi                                   | Momentum   | $2.0 \times 10^5$                   | 2.0                          | 0.15                          | Primordial |
| RefNorm 10 <sup>5</sup>       | 10 <sup>5</sup> | Yes        | Default Bondi                                   | Duty Cycle | $2.0 \times 10^5$                   | 2.0                          | 0.15                          | Primordial |
| RefNorm 10 <sup>5</sup>       | 10 <sup>5</sup> | Yes        | Default Bondi                                   | Bipolar    | $2.0 \times 10^5$                   | 2.0                          | 0.15                          | Primordial |
| RefNorm 10 <sup>5</sup>       | 10 <sup>5</sup> | Yes        | Default Bondi                                   | Bipolar    | $2.0 \times 10^5$                   | 2.0                          | 0.15                          | + Metals   |
| Fixed RefNorm 10 <sup>5</sup> | 10 <sup>5</sup> | Yes        | $\dot{M}_{\text{BH}} = 0.1\dot{M}_{\text{Edd}}$ | Thermal    | $2.0 \times 10^5$                   | 2.0                          | 0.15                          | Primordial |
| Fixed RefNorm 10 <sup>5</sup> | 10 <sup>5</sup> | Yes        | $\dot{M}_{\text{BH}} = 0.1\dot{M}_{\text{Edd}}$ | Momentum   | $2.0 \times 10^5$                   | 2.0                          | 0.15                          | Primordial |
| Fixed RefNorm 10 <sup>5</sup> | 10 <sup>5</sup> | Yes        | $\dot{M}_{\text{BH}} = 0.1\dot{M}_{\text{Edd}}$ | Duty Cycle | $2.0 \times 10^5$                   | 2.0                          | 0.15                          | Primordial |
| Fixed RefNorm 10 <sup>5</sup> | 10 <sup>5</sup> | Yes        | $\dot{M}_{\text{BH}} = 0.1\dot{M}_{\text{Edd}}$ | Bipolar    | $2.0 \times 10^5$                   | 2.0                          | 0.15                          | Primordial |
| Fixed RefNorm 10 <sup>5</sup> | 10 <sup>5</sup> | Yes        | $\dot{M}_{\text{BH}} = 0.1\dot{M}_{\text{Edd}}$ | Bipolar    | $2.0 \times 10^5$                   | 2.0                          | 0.15                          | + Metals   |

**Table 3.** Simulation details of isolated disc galaxy models. We list the name of the simulation that we use throughout this paper, as well as the initial number of resolution elements. Note that for all simulations, and especially those with refinement, the number of gas cells will increase from this initial value. In column 4 we indicate the accretion rate prescription we use, as well as the feedback mechanism in column 5. In columns 6-8 we list the target gas mass of the simulation (that is set to be the initial gas cell mass) as well as the dark matter and gas smoothing lengths. Note that in the course of simulations the gas gravitational softening is adaptive and is set to the maximum of  $\epsilon_{\text{gas}}$  and 2.5 times the cell size. The last column indicates simulations where we include metal line cooling additionally to the primordial cooling.

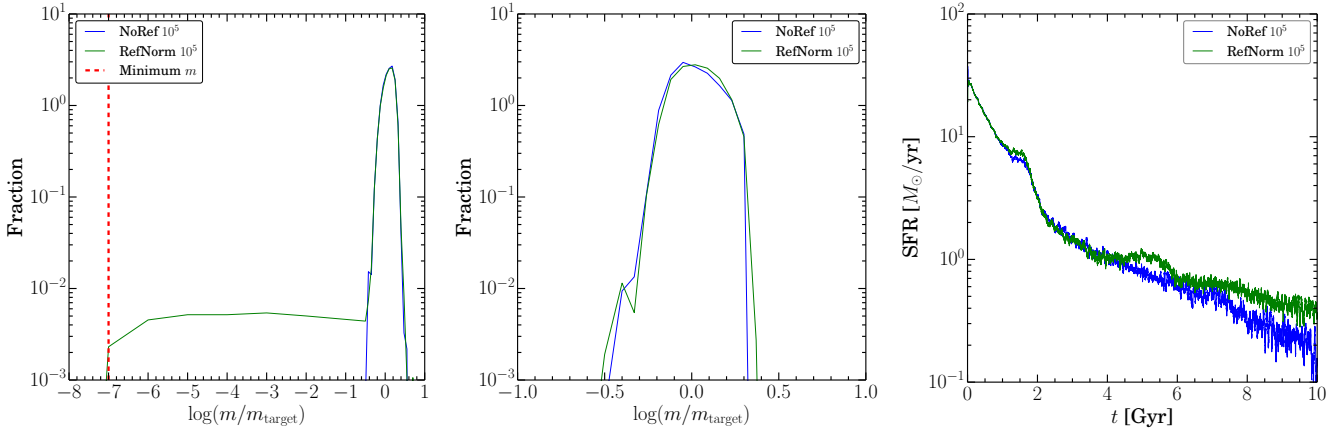


**Figure 6.** Effects of the refinement technique. In the left-hand panel we plot the mass distribution of the gas cells, comparing that for our simulations without and with refinement. The distributions are in very good agreement at the high mass end, which demonstrates that we are not de-refining cells unnecessarily. At the low mass end, our refinement scheme results in an increased number of smaller mass cells, as expected. This drops off at the minimum cell mass, which we denote with a vertical red line. Similarly, in the central panel we show the distribution of stellar particle masses. Here, the distribution is the same for the case with refinement as that without refinement. We suppress star formation in the refinement region, which prevents smaller star particles from being formed, which could cause unwanted numerical heating. In the right-hand panel, we show the time evolution of star formation rates with and without our refinement scheme. The star formation rates are broadly the same regardless of the refinement scheme being used or not, with the slightly larger star formation rates at late times in the refinement case caused by the slightly lower rate of accretion onto the central black hole (see Figure 10).

scheme affects the gas cell size. Here, we plot the minimum (blue), maximum (green) and mean (red) of the cell radii within the black hole smoothing length,  $h_{\text{BH}}$ , which we also show (purple). We compare these to the instantaneous Bondi radius,  $r_{\text{B}}$ , (cyan) over the whole duration of the run, i.e.  $t = 10$  Gyr. With our choice of parameters the refinement region spans  $0.5 - 1$  kpc in radius, the mean cell size within the refinement region is of the order of  $0.05 - 0.1$  kpc, while the minimum cell radius  $r_{\text{min}} \leq 2r_{\text{B}}$  for the majority of the

simulation timespan. This implies that we are not only probing the spatial regions very close to the Bondi radius, but that we are also resolving much better the gas structure in its surroundings which helps to estimate more accurately the gas density and sound speed that are used in equation 5.

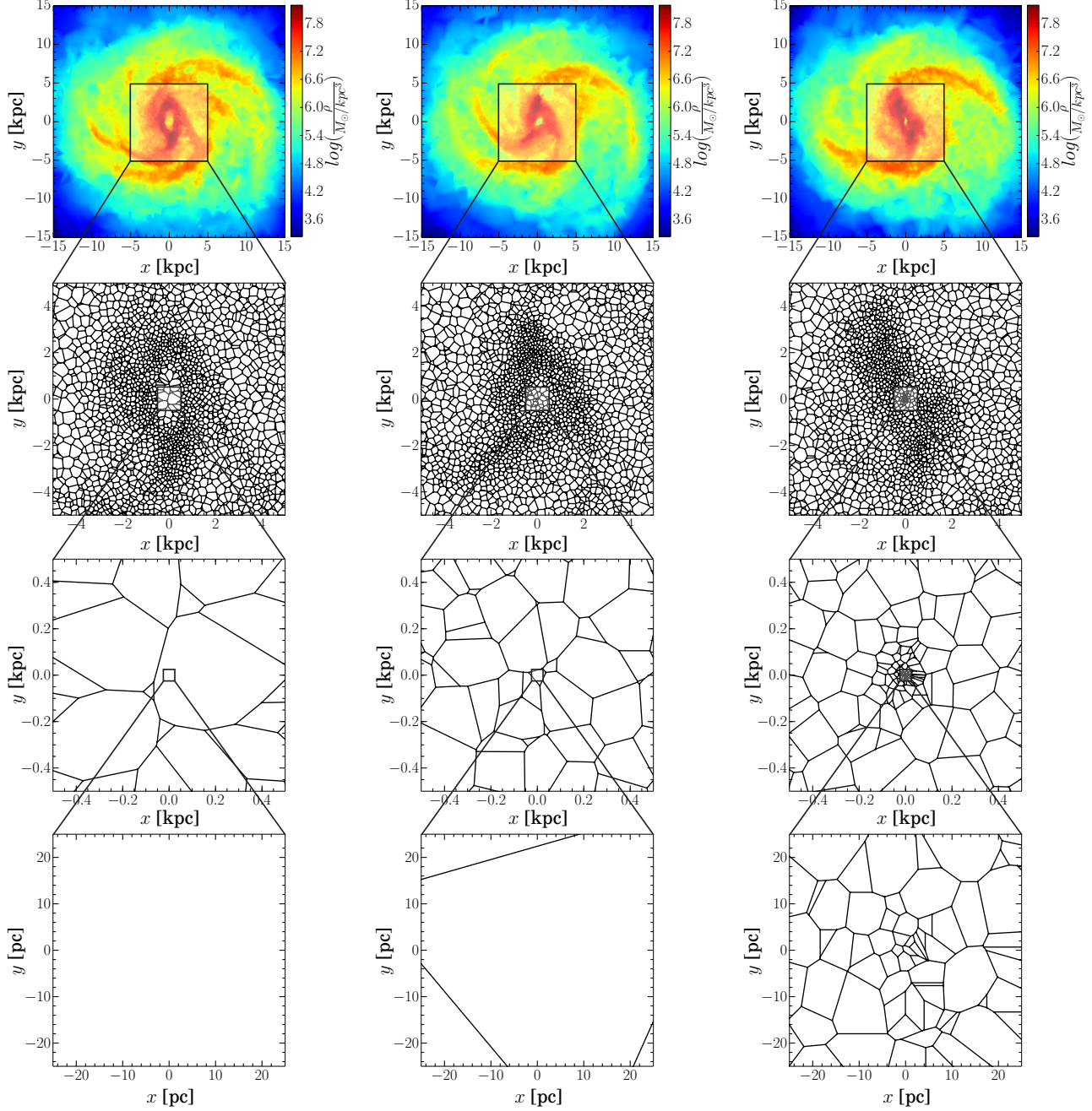


**Figure 8.** Illustrations of our refinement method. All images show the Voronoi mesh, with cells coloured according to the gas density on the large scale plots in the top panels. The top row shows slices throughout the  $x - y$  plane in the central  $30 \text{ kpc} \times 30 \text{ kpc}$  region centred on the black hole. The bottom rows show a zoomed-in plots of the central  $10 \text{ kpc} \times 10 \text{ kpc}$ ,  $1 \text{ kpc} \times 1 \text{ kpc}$  and  $50 \text{ pc} \times 50 \text{ pc}$  region, respectively. The first column shows the case for no refinement, whilst the second column shows the same, but for a simulation including moderate refinement with parameters  $R_{\text{ref}} = h_{\text{BH}}$ ,  $R_{\text{cell}}^{\text{max}} = 0.5h_{\text{BH}}$ ,  $R_{\text{cell}}^{\text{min}} = 10r_{\text{B}}$ , with  $M_{\text{min}} = 10^2 M_{\odot}$ . Third column shows a simulation with more aggressive parameters  $R_{\text{ref}} = h_{\text{BH}}$ ,  $R_{\text{cell}}^{\text{max}} = 0.5h_{\text{BH}}$ ,  $R_{\text{cell}}^{\text{min}} = r_{\text{B}}$ , with  $M_{\text{min}} = 10^{-2} M_{\odot}$ .

#### 4.3 The effect on gas properties and black hole growth

Figure 8 shows how our refinement scheme works in practice. In the top panels we plot the large scale gas density distribution in a box of  $30 \text{ kpc}$  on a side, while in rows 2, 3 and 4 we show the Voronoi tessellation across the  $x - y$  plane as we zoom-in towards the central black hole. The left-

hand panel shows the results for a standard simulation when our black hole refinement scheme is turned off. As the black hole accretes matter, energy is injected into the surrounding gas cells, increasing their temperature and decreasing their density. The code maintains approximately constant mass cells, so they necessarily increase in volume. This significantly coarsens the resolution around the central region.

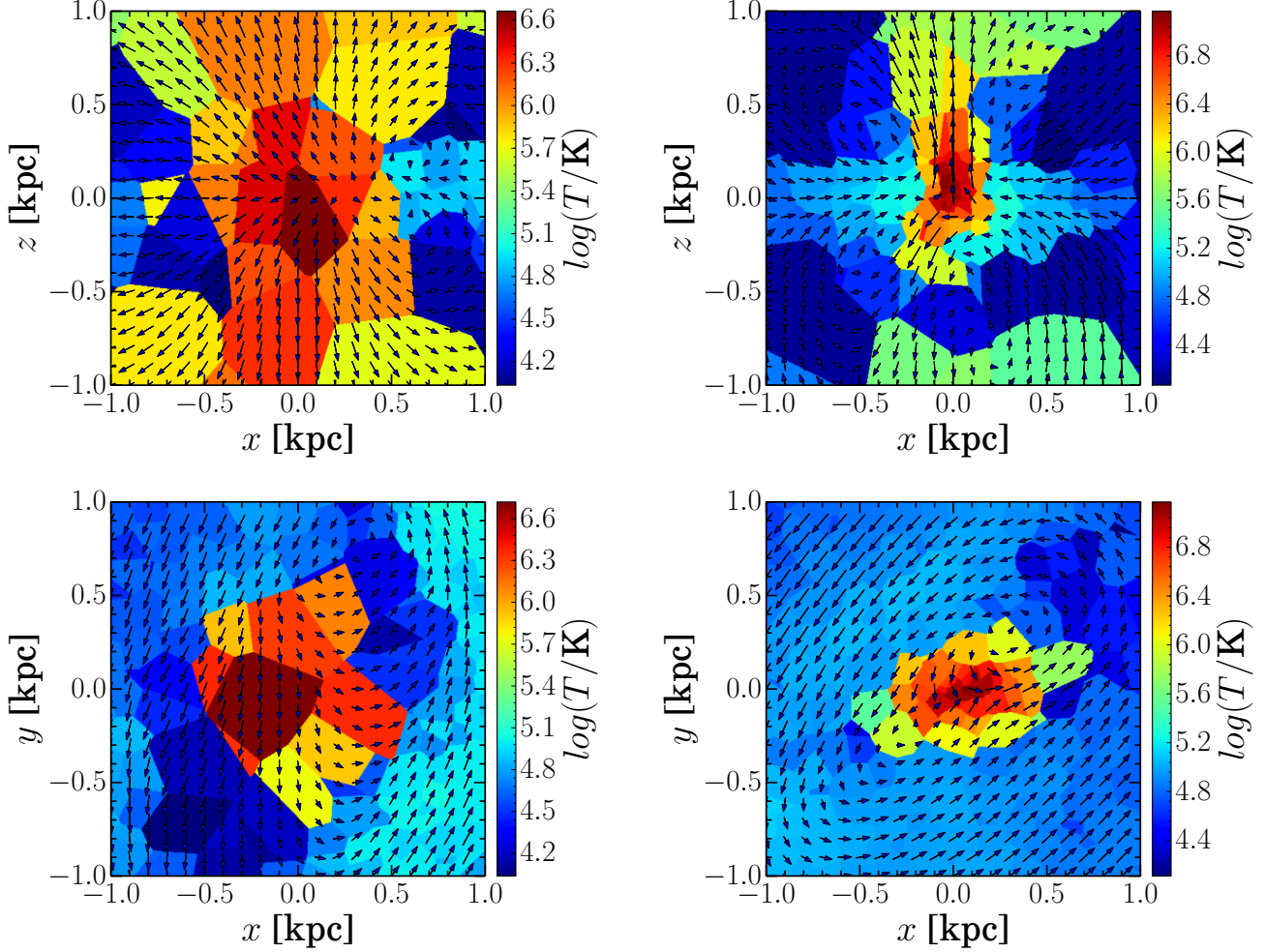


**Figure 9.** Temperature maps of the gas in the central region for simulations without (left-hand panels) and with (right-hand panels) super-Lagrangian refinement using thermal feedback. Each Voronoi cell is coloured according to the mean gas temperature within the cell. Overplotted arrows indicate the direction and relative speed of the gas flow. The mean arrow size corresponds to  $\sim 80 \text{ km s}^{-1}$  while the largest arrows are for  $\sim 200 \text{ km s}^{-1}$  in the left-hand panels, and  $\sim 300 \text{ km s}^{-1}$  in the right-hand panels. In the top row, we show a slice through the  $x - z$  plane centred on the black hole (edge-on view) at a time of 1.5 Gyr. Here, we see the effect of feedback on the velocity of the gas, causing it to buoyantly rise perpendicular to the disc before settling back down at larger radii. In the non-refined simulation, the feedback heated gas dominates the central region whilst, in the refined simulation, the cold gas component that forms the outer accretion disc is clearly evident. This can also be seen in the bottom row, where we plot a slice through the  $x - y$  plane centred on the black hole (face-on view) at 1.0 Gyr, before the disc is significantly disrupted. Here, we can see how the rotation structure of the gas is affected by the presence of the feedback, with the non-refined case again suffering from resolution problems in the central most region.

This is a numerical problem present in all simulation codes which maintain roughly constant mass cells (or particles, i.e. in SPH) and/or which do not refine regions around black holes specifically to cure this problem (see also Vogelsberger et al. 2013). As such, the vast majority of simulations in the literature suffer from the same effect.

In the middle and right-hand panels, we show the same situation with our refinement scheme turned on. Here, the lower density cells caused by the feedback are still evident, but the region affected is much smaller. Indeed, in the simulation with more aggressive refinement parameters (right-hand panels), while the large scale fluid properties are the same, the structure of the innermost gas is very different -

the edge of the hot bubble is resolved, and higher density gas is able to reach closer to the black hole and accrete.

Figure 9 shows the effect that our refinement technique has on the central velocity and temperature structure. We show the temperature of the Voronoi mesh cells present in a slice in the region around the black hole for simulations using the thermal feedback prescription. The arrows overlaying each plot show the velocity field of the gas cells, interpolated over the slice. The top row shows slices through the  $x - z$  plane (edge-on view). Here, we see the effect of the thermal feedback in heating bubbles of gas that are forced to rise buoyantly out of the disc. This is to be contrasted with the cold disc present in the  $z = 0$  plane, which is an extension of the gaseous disc on large scales and which provides the



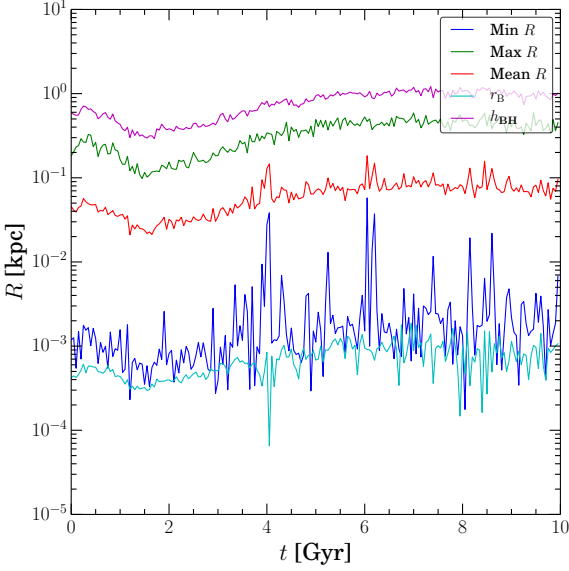


**Figure 7.** The distribution of cell radii within the refinement region. Here we show the minimum (blue), the maximum (green) and the mean (red) cell radii for cells within the refinement region as a function of time. We also show  $r_B$  as a function of time (cyan). Our refinement parameters here are  $R_{\text{ref}} = h_{\text{BH}}$ ,  $R_{\text{cell}}^{\text{max}} = 0.5h_{\text{BH}}$  and  $R_{\text{cell}}^{\text{min}} = r_B$ , where  $h_{\text{BH}}$  is the black hole smoothing length (purple).

dense gas responsible for feeding the black hole. There is a stark difference over the central region - in the non refined case the feedback overwhelms the central region, with cells ballooning out of the disc. In particular, much of the structure of the outflow in the region closest to the black hole is unresolved. This can be contrasted with the refinement simulation, where the cold gaseous disc is significant down to scales much closer to the black hole. The feedback driven outflow is also better resolved. The bottom row shows similar plots for the  $x - y$  plane (face-on view). In both cases, there is evidence of rotation and a centrifugally supported disc. We can see that in the refinement case, however, the disc is better resolved, and the refinement prevents the feedback from destroying this structure. In addition, the central low density bubble is much smaller in the refinement case.

In Figure 10, we show the effect of our refinement technique on the mass growth rate of the black hole, for simulations with thermal feedback. The simulations with refinement show somewhat lower rates of gas accretion than those without. This can be explained in terms of the scheme's impact on the estimated fluid parameters for the region surrounding the black hole. There are two clear effects. First, the density of the fluid in the region around the black hole, outside of the very centre, is higher. This is expected and is because by increasing the local resolution, we are able to resolve higher densities of accreting gas rather than smearing the same mass out over larger cell sizes. However, the second effect is a consequence of depositing the feedback energy into smaller cells. These rise to a higher temperature, meaning that the sound speed is always above that for the non refined case. This effect leads to a lowering of the den-

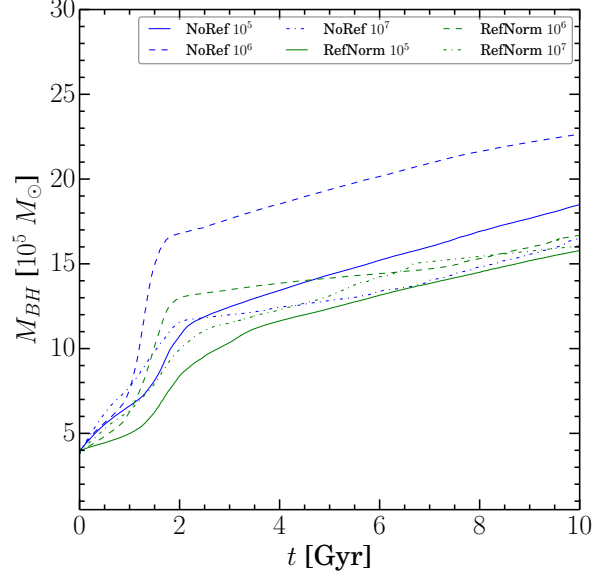


**Figure 10.** The evolution of the black hole mass as a function of time for simulations with no refinement (blue) and with refinement (green) for three different resolutions ( $10^5$ ,  $10^6$  and  $10^7$  initial gas cells). All simulations here use the thermal feedback prescription. The convergence properties of super-Lagrangian refinement simulations are better, as expected.

sity in the very centre of the simulation and a subsequent suppression of the accretion rate. The change is however not exceptionally large: this is because in this basic implementation of feedback we are unable to take advantage of all of the improved resolution that refinement gives. In addition to these differences, the simulations with refinement show better convergence rate than those without. This is encouraging and, agreeing with the results of our Bondi inflow simulations, suggests that our refinement technique will allow future cosmological simulations to have better convergence properties, which is vital if they are to have higher predictive power.

## 4.4 Changing the Feedback

### 4.4.1 The role of feedback

To understand exactly how our refinement scheme affects the structure of the gas, as well as how the choice of different feedback routines combine with this, we need to isolate the effect of the injection of the feedback itself from the subsequent coupled effect that this has on the sound speed and density of the gas and, as a result, on the accretion rate itself. To this end, we run a set of simulations of our isolated galaxy models, but with the black hole accreting at a fixed, constant accretion rate. It is important that this rate is not too high, or the surrounding gas will be blown away on a short time-scale, or too low, which will result in the different feedback algorithms being indistinguishable. We find that a value of  $\dot{M}_{\text{BH}} = 0.1\dot{M}_{\text{Edd}}$  (for the initial mass of the black hole) allows for this balance. We compare the impact of the feedback on the surrounding gas when using either the thermal or the momentum injection algorithms described above, and also how this changes when the feedback is injected over

a duty cycle. We also investigate how using our new bipolar model of feedback changes the gas parameters.

#### 4.4.2 The effect on gas properties

The most direct impact that the choice of feedback algorithm has is on the temperature of the gas and, subsequently, the sound speed. We find that the difference between the largest (simple, isotropic thermal feedback) and the lowest (bipolar feedback with metal line cooling, or thermal feedback injected in a duty cycle fashion) is consistently around a factor of 10 as shown in the left-hand panel of Figure 11. The green and blue lines show the sound speed for simple, isotropic thermal feedback for simulations with and without our refinement technique, respectively. Here, the masses of the cells in the centre of the refinement simulation are much smaller. As such, although the amount of energy distributed is the same, the peak temperature reached in these cells is much higher which, even when averaged over the smoothing length of the black hole, results in a higher sound speed. When momentum feedback (the red line) is used, the result is different - the gas is shock heated by secondary processes when the accelerated gas collides with accreting material. This results in a consistently much smaller sound speed. Indeed, we find that when using momentum feedback the black hole accretion is eventually shut off by a burst of feedback sufficient to dramatically reduce the density of the gas in the centre of the galaxy, rather than by increasing the sound speed (which dampens the accretion rate). Unsurprisingly, our simulations using bipolar feedback, both with and without metal line cooling, result in a consistently lower sound speed. Similarly, whilst the duty cycle run shows bursts aligned with each injection of feedback, the energy is quickly transported away and the overall sound speed is much lower than the standard thermal injection.

This raises a further point - that in addition to the rise in temperature of the gas, the subsequent accumulation or transportation of feedback energy is sensitive to the feedback routine. In the thermal feedback case, the sound speed of the gas close to the black hole steadily rises over the course of 1 Gyr, whilst for the other routines it is nearly constant. This implies a further compound effect that the feedback algorithm choice has in less controlled simulations.

It might be argued that, in practice, this will not affect the average black hole accretion rate over the relevant time-scales of galaxy formation because the accretion will enter a self-regulation phase - more powerful feedback will shut off the accretion on to the black hole, removing the energy for the feedback. We discuss the black hole accretion itself in the section below, however it is worth noting here that, even if this is the case for the commonly used Bondi accretion rate, when we consider the impact of gas angular momentum then the sound speed itself will take on a new importance. The magnitude of the effect of angular momentum is likely to be highly dependent on the sound speed of the gas: at high sound speeds, this effect is likely to be substantially decreased. We will discuss this in further detail in our next paper. Furthermore, when using our bipolar model, feedback has only an indirect effect on the accreting material, which results by construction in the simulation never quite achieving a steady self-regulation phase.

In the right-hand panel of Figure 11 we show the evolu-

tion of the density of the gas surrounding the black hole. The impact here is generally similar to that on the sound speed, but with some important differences. The thermal feedback causes a steady decrease in the density of the gas around the black hole, both due to the increase in temperature but also because mass is transported away, as hot gas rises buoyantly out of the galaxy. The same is true for the duty cycle feedback. The momentum feedback has the smallest effect on the density, because the momentum kicks given to the surrounding gas (whose strength are tied to the black hole mass) are insufficient to overcome the accreting material. Both bipolar models show similar behaviour in maintaining a higher density for a longer period of time into the simulation, because the feedback is restricted to a cone and as such the accreting material does not fall off in density as quickly. When metal line cooling is included, this effect is magnified as the cold disc becomes denser throughout the simulation, offsetting the effects of the feedback.

Left-hand panel of Figure 12 shows a similar plot of the sound speed of the gas in the vicinity of the black hole, but this time for simulations with self-consistent black hole accretion and feedback rates. Here, the sound speed of the gas is on the whole much lower and the differences between the different feedback regimes are not as pronounced. This is the evidence of self-regulation - the overall amount of feedback is lower because any increase in the sound speed shuts off accretion. Note that, despite this, there are still notable differences in the sound speed - up to a factor of 4, which as previously discussed are still very important in the context of considering angular momentum. Furthermore, there can still be large differences in the final mass of the black hole, even when the sound speeds are similar, as we will discuss next.

#### 4.4.3 The consequences for black hole growth

In the right-hand panel of Figure 12, we look at how the choice of feedback algorithm affects the black hole growth. The first thing to note is that the algorithm itself has the largest single impact on the final mass of the black hole. In particular, for our simulation with momentum feedback, which does not directly heat the gas, the black hole grows at a high accretion rate until the momentum feedback is powerful enough to drive a shell out of the centre of the galaxy, which shuts off the accretion but only after the black hole has grown by many orders of magnitude. In the duty cycle case, the final mass of the black hole is an order of magnitude higher than that in the isotropic, thermal case. This is largely the effect of the substantially smaller sound speed of the gas, which dominates over the density in the accretion rate, as well as the fact that when not Eddington limited the black hole grows as  $\sim M_{\text{BH}}^2$ , so any early differences are magnified at later times. Perhaps equally important, however, is that if we do not assume isotropy and break the direct connection between the outflowing, feedback heated gas and the cold accreting gas that feeds the black hole, we weaken the ease with which the black hole can fall into a stable self-regulated regime.

However, even though the black hole ends up at a similar mass for the simulations with thermal and bipolar feedback, the growth history and, as noted before, the gas properties are markedly different. A further example of this can



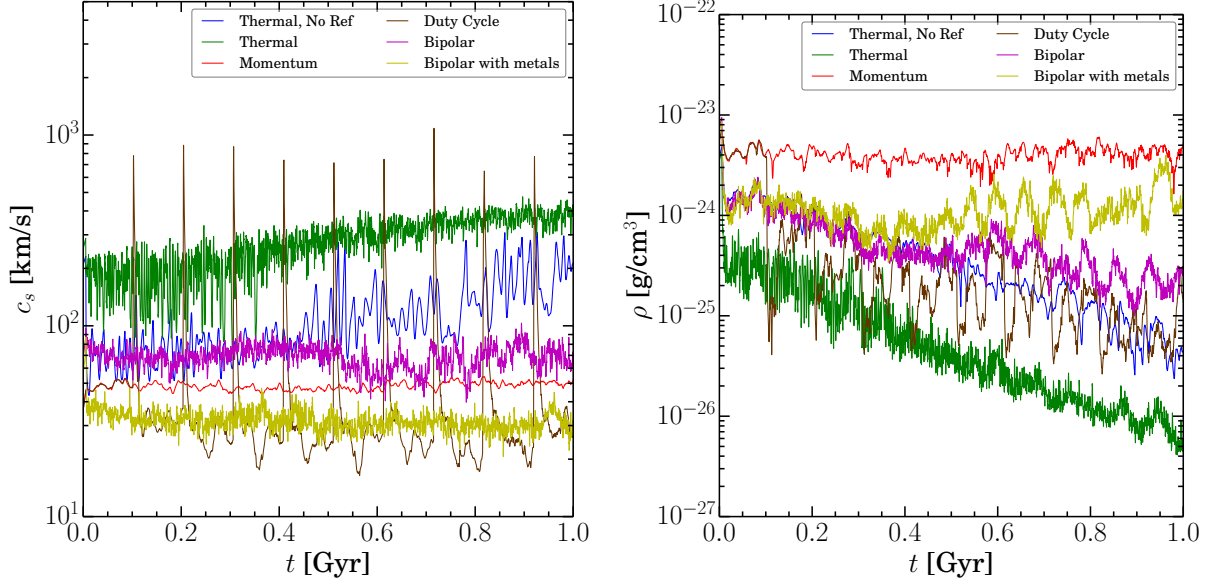


**Figure 11.** The effect of the feedback algorithm on the sound speed and density of the gas. In the left-hand panel, we show the evolution of the sound speed of the gas and in the right-hand panel, we show the same for the density of the gas. In both cases, the value shown is that used in our estimation of the accretion rate, i.e. averaged over the smoothing length of the black hole. In blue, we show the case for thermal feedback with no refinement and in green that for thermal feedback but with refinement. We show the case for momentum feedback in red and in brown we show that for duty cycle feedback. We also show the results for our non isotropic model, both with (gold) and without (purple) metal line cooling enabled.

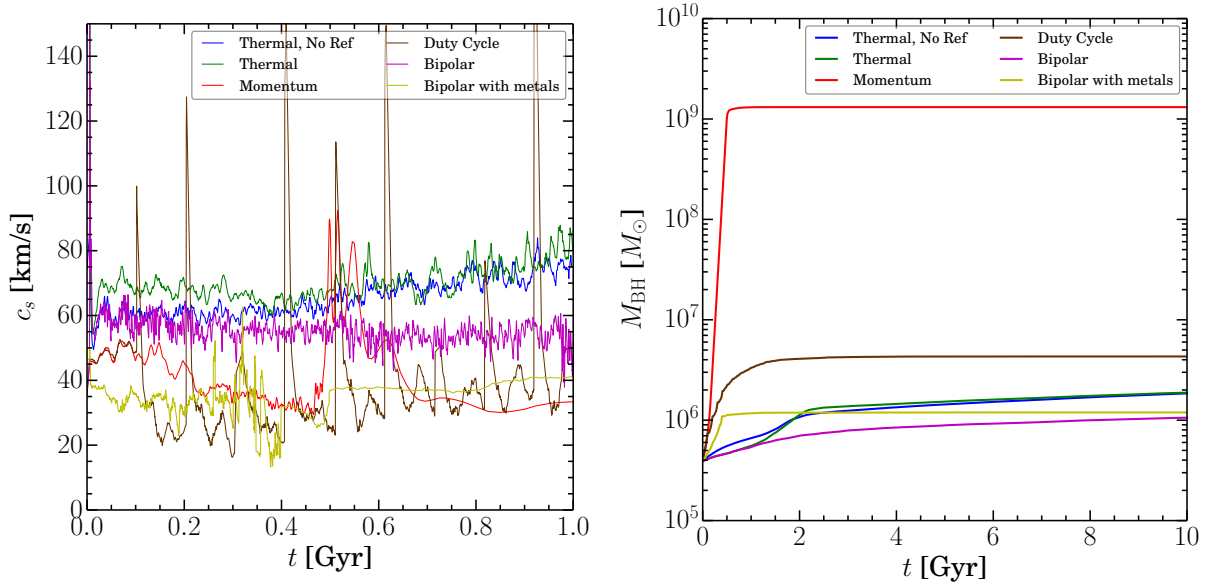


**Figure 12.** The effect of the feedback algorithm in self-consistent simulations. On the left, as in Figure 11, we show how the sound speed evolves with time for different feedback routines, but now with self-consistent black hole accretion rate prescription. On the right we show the corresponding evolution of the black hole mass over the full 10 Gyrs of time evolution.

be seen in Figure 13, in which we show the probability density function of the radial velocity of gas in the same set of simulations. In particular, this allows us to characterize the properties of the outflow for different types of feedback that, in principle, may provide a very useful diagnostics once compared to observations. In the left-hand panel we show the radial velocity at  $t = 0.25$  Gyr and on the right that

at  $t = 0.5$  Gyr. In both cases, the simple thermal feedback fails to drive a significant outflow. We find that this does eventually emerge, but only after longer periods of time. By contrast the run with bipolar feedback drives an outflow from early times, an effect that is magnified when metal line cooling is included. In the duty cycle case, too, there is a large proportion of fast outflowing material at  $t = 0.25$  Gyr,

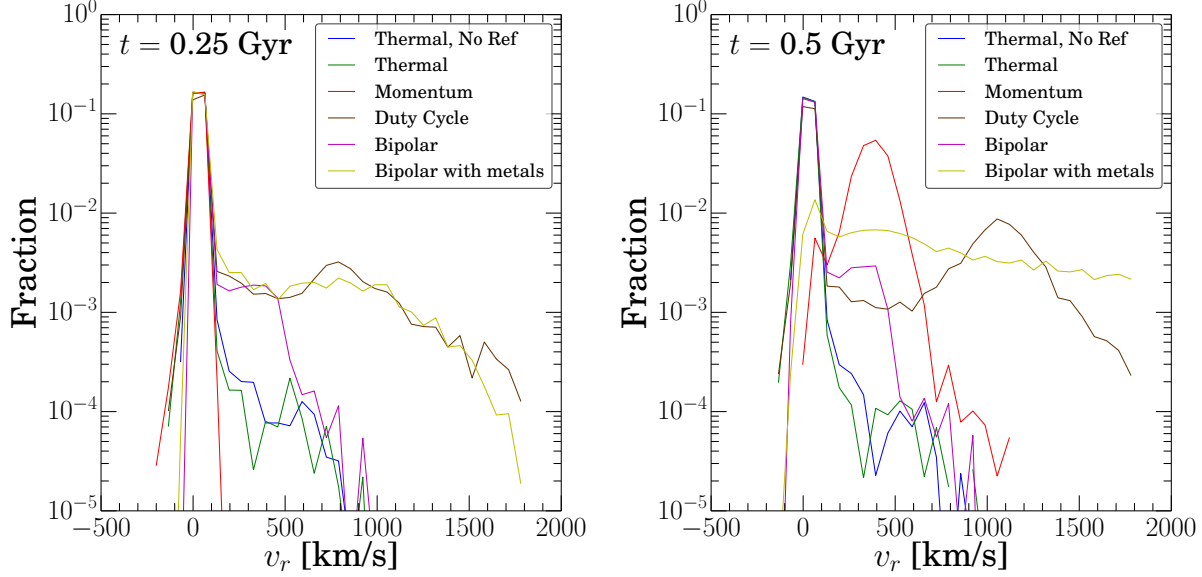


**Figure 13.** Radial velocity probability density functions for simulations with different types of feedback, with self-consistent black hole accretion. Positive velocities indicate material moving away from the black hole. Left-hand panel is for  $t = 0.25$  Gyr, while on the right  $t = 0.5$  Gyr. At early times, there is no significant outflow for the thermal or momentum models, whilst the bipolar and the duty cycle models show high velocity outflowing material. At the later time, the black hole now has sufficient mass that in the momentum case (red) the feedback is able to drive a high velocity shell of material that can be clearly seen peaking around  $400 \text{ km s}^{-1}$ . The differences in gas properties of simulated galaxies may provide a powerful method for constraining the feedback mechanism when these are compared to observed galaxies.

whilst the outflow in the momentum feedback run is minimal. This changes at  $t = 0.5$  Gyr - at this point, the black hole has sufficient mass to drive an outflow that removes gas from the centre of the galaxy in a fast moving shell that can be clearly seen, peaking at around  $400 \text{ km s}^{-1}$ . The effect of this can be seen in the clear shut off of the accretion rate in Figure 12. By comparing these figures, we also see that the accretion for the duty cycle run and bipolar run with metal line cooling has all but dried up by 0.5 Gyr and that both show a large amount of material in a corresponding outflow. In these cases, the discrete, large injections of energy in the duty cycle case lead to an outflow bunched around a peak velocity of around  $1200 \text{ km s}^{-1}$ , whilst the continuous feedback of the bipolar outflow leads to an extended distribution across a wide velocity range. By looking at the outflowing mass as a function of radius, we can confirm this effect - for the bipolar simulation, mass is outflowing for a wide range of radii, whilst the duty cycle simulation only shows fast moving shells of mass ejected from the central region. This indicates that by investigating the fraction of galaxies with outflows at specified radii we may be able to constrain the nature of feedback.

## 5 CONCLUSIONS

In this paper we have presented a new scheme for increasing the resolution around black holes in a super-Lagrangian fashion in full hydrodynamical simulations of galaxy formation. Our scheme adaptively targets on-the-fly spatial regions around black holes where the resolution is increased

progressively up to the desired minimum spatial scales without introducing any unwanted boundary effects.

We have implemented our scheme in the moving mesh code AREPO. We demonstrated that our refinement technique is able to reproduce the theoretical Bondi rate at lower resolutions than otherwise possible and that we are able to match higher resolution runs with lower CPU costs. We have also demonstrated the flexibility of our technique and that using more aggressive refinement parameters leads to a closer agreement with the theoretical predictions, at a cost of increased CPU resources. Our work opens the possibility that in future we will be able to perform simulations of black hole accretion by allowing black holes to swallow material directly using a sink particle-like routine in combination with a small-scale sub-grid model for accretion (without the need to estimate the Bondi rate), a technique which has previously been prone to high stochasticity and inaccuracies.

We have studied the effects of our novel implementation in simulations of isolated Milky Way-like galaxy models. We found that our refinement technique is able to increase the resolving power around the central black hole by up to seven orders of magnitude in mass resolution, reaching scales of order of the Bondi radius for the whole duration of simulations of 10 Gyrs. This allowed us to resolve more accurately the gas properties in the vicinity of the black hole and thus to estimate the accretion rate more robustly. We stress however that that our accretion rate estimate still depends on the sub-grid model employed which is parameterized via Bondi-Hoyle-like accretion (see equation 5).

Taking advantage of our novel refinement method we have implemented several different mechanisms of injecting black hole feedback, including the injection of mass, ther-

mal energy and/or momentum in both isotropic and non-isotropic distributions. We found that the choice of feedback algorithm can have a very large effect both on the characteristics of the gas in the central region of our simulated galaxies as well as on large scales, and, consequently, on the growth history of the central black hole. Specifically, we found that momentum-only feedback leads to a growth of overmassive black holes before the gas can be efficiently expelled from the central region of the galaxy (see also Costa et al. 2014). Instead, feedback schemes that incorporate at the same time mass, energy and momentum injection in conjunction with cooling to low temperatures via metals seem most promising in generating both realistic black hole masses and persistent large-scale outflows with velocities up to  $1500 \text{ km s}^{-1}$ .

The obvious next step for future work will be to look at the observational characteristics of the different feedback mechanisms in full cosmological simulations, which will be required to properly quantify the differences outlined above in a realistic environment. As ALMA observations continue, and as multiple integral field unit (IFU) surveys (e.g. MaNGA, SAMI, CALIFA, Atlas3D) release their data we will, in the near future, have unprecedented detail of individual galaxies as well as much larger statistical samples of galaxies. These data will provide new constraints on black hole feedback processes. Computational models of AGN feedback will have to continue to move beyond matching black hole scaling relations and large scale galaxy properties towards reproducing the detailed thermo-dynamical properties of galaxies, if we are to make use of the constraining power of the new data available. Our super-Lagrangian refinement method will allow us to more reliably track black hole accretion and feedback in full cosmological simulations and thus to gain further insight into the growth history of galaxies and supermassive black holes in our Universe.

## ACKNOWLEDGEMENTS

We thank Martin Haehnelt, Ewald Puchwein, Chris Reynolds and Volker Springel for their useful comments and advice. MC is supported by the Science and Technology Facilities Council (STFC). This work was performed on the following: the COSMOS Shared Memory system at DAMTP, University of Cambridge operated on behalf of the STFC DiRAC HPC Facility - this equipment is funded by BIS National E-infrastructure capital grant ST/J005673/1 and STFC grants ST/H008586/1, ST/K00333X/1; DiRAC Darwin Supercomputer hosted by the University of Cambridge High Performance Computing Service (<http://www.hpc.cam.ac.uk/>), provided by Dell Inc. using Strategic Research Infrastructure Funding from the Higher Education Funding Council for England and funding from the Science and Technology Facilities Council; DiRAC Complexity system, operated by the University of Leicester IT Services, which forms part of the STFC DiRAC HPC Facility ([www.dirac.ac.uk](http://www.dirac.ac.uk)). This equipment is funded by BIS National E-Infrastructure capital grant ST/K000373/1 and STFC DiRAC Operations grant ST/K0003259/1. DiRAC is part of the National E-Infrastructure.

## REFERENCES

- Anglés-Alcázar D., Özel F., Davé R., 2013, *ApJ*, 770, 5  
 Barai P., Proga D., Nagamine K., 2011, *MNRAS*, 418, 591  
 Bauer A., Springel V., 2012, *MNRAS*, 423, 2558  
 Bondi H., 1952a, *MNRAS*, 112, 195  
 Bondi H., 1952b, *MNRAS*, 112, 195  
 Booth C. M., Schaye J., 2009, *MNRAS*, 398, 53  
 Chapon D., Mayer L., Teyssier R., 2013, *MNRAS*, 429, 3114  
 Choi E., Ostriker J. P., Naab T., Johansson P. H., 2012, *ApJ*, 754, 125  
 Choi E., Ostriker J. P., Naab T., Oser L., Moster B. P., 2014, *MNRAS* submitted, arXiv:1403.1257  
 Cicone C. et al., 2014, *A&A*, 562, A21  
 Costa T., Sijacki D., Haehnelt M. G., 2014, *MNRAS*, 444, 2355  
 Debuhr J., Quataert E., Ma C.-P., 2011, *MNRAS*, 412, 1341  
 Di Matteo T., Springel V., Hernquist L., 2005, *Nature*, 433, 604  
 Dubois Y., Devriendt J., Slyz A., Teyssier R., 2012, *MNRAS*, 420, 2662  
 Fabian A. C., 1999, *MNRAS*, 308, L39  
 Fabian A. C., 2012, *ARA&A*, 50, 455  
 Fabian A. C., Sanders J. S., Taylor G. B., Allen S. W., Crawford C. S., Johnstone R. M., Iwasawa K., 2006, *MNRAS*, 366, 417  
 Ferrarese L., Merritt D., 2000, *ApJ*, 539, L9  
 Forman W. et al., 2007, *ApJ*, 665, 1057  
 Gebhardt K. et al., 2000, *ApJ*, 539, L13  
 Genzel R. et al., 2014, *ApJ*, 796, 7  
 Gültekin K. et al., 2009, *ApJ*, 698, 198  
 Hernquist L., 1990, *ApJ*, 356, 359  
 Hobbs A., Power C., Nayakshin S., King A. R., 2012, *MNRAS*, 421, 3443  
 Hopkins P. F., Quataert E., 2011, *MNRAS*, 415, 1027  
 Jiang Y.-F., Stone J. M., Davis S. W., 2014, *ApJ*, 796, 106  
 Kawata D., Gibson B. K., 2005, *MNRAS*, 358, L16  
 Kereš D., Vogelsberger M., Sijacki D., Springel V., Hernquist L., 2012, *MNRAS*, 425, 2027  
 King A., 2005, *ApJ*, 635, L121  
 King A. R., Pringle J. E., 2007, *MNRAS*, 377, L25  
 Kitsionas S., Whitworth A. P., 2002, *MNRAS*, 330, 129  
 Kormendy J., Ho L. C., 2013, *ARA&A*, 51, 511  
 Kormendy J., Richstone D., 1995, *ARA&A*, 33, 581  
 Krumholz M. R., McKee C. F., Klein R. I., 2005, *ApJ*, 618, 757  
 Krumholz M. R., McKee C. F., Klein R. I., 2006, *ApJ*, 638, 369  
 Kurosawa R., Proga D., 2009, *MNRAS*, 397, 1791  
 Levine R., Gnedin N. Y., Hamilton A. J. S., 2010, *ApJ*, 716, 1386  
 Lynden-Bell D., 1969, *Nature*, 223, 690  
 Magorrian J. et al., 1998, *AJ*, 115, 2285  
 Maiolino R. et al., 2012, *MNRAS*, 425, L66  
 Marconi A., Hunt L. K., 2003, *ApJ*, 589, L21  
 Martel H., Evans, II N. J., Shapiro P. R., 2006, *ApJS*, 163, 122  
 Mayer L., Fiacconi D., Bonoli S., Quinn T., Roškar R., Shen S., Wadsley J., 2015, *ApJ*, 810, 51  
 McConnell N. J., Ma C.-P., 2013, *ApJ*, 764, 184

Monaghan J. J., Lattanzio J. C., 1985, *A&A*, 149, 135  
 Navarro J. F., Frenk C. S., White S. D. M., 1996, *ApJ*, 462, 563  
 Ostriker J. P., Choi E., Ciotti L., Novak G. S., Proga D., 2010, *ApJ*, 722, 642  
 Pakmor R., Springel V., Bauer A., Mocz P., Munoz D. J., Ohlmann S. T., Schaal K., Zhu C., 2015, *ArXiv e-prints*  
 Pounds K. A., Reeves J. N., King A. R., Page K. L., O'Brien P. T., Turner M. J. L., 2003, *MNRAS*, 345, 705  
 Power C., Nayakshin S., King A., 2011, *MNRAS*, 412, 269  
 Rosas-Guevara Y. M. et al., 2015, *MNRAS*, 454, 1038  
 Rupke D. S. N., Veilleux S., 2011, *ApJ*, 729, L27  
 Sijacki D., Springel V., Di Matteo T., Hernquist L., 2007, *MNRAS*, 380, 877  
 Sijacki D., Springel V., Haehnelt M. G., 2011, *MNRAS*, 414, 3656  
 Sijacki D., Vogelsberger M., Kereš D., Springel V., Hernquist L., 2012, *MNRAS*, 424, 2999  
 Silk J., Rees M. J., 1998, *A&A*, 331, L1  
 Springel V., 2010, *MNRAS*, 401, 791  
 Springel V., Di Matteo T., Hernquist L., 2005, *MNRAS*, 361, 776  
 Springel V., Hernquist L., 2003, *MNRAS*, 339, 289  
 Sturm E. et al., 2011, *ApJ*, 733, L16  
 Teyssier R., 2002, *A&A*, 385, 337  
 Tombesi F., Melendez M., Veilleux S., Reeves J. N., Gonzalez-Alfonso E., Reynolds C. S., 2015, *arXiv:1501.07664*  
 Torrey P., Vogelsberger M., Sijacki D., Springel V., Hernquist L., 2012, *MNRAS*, 427, 2224  
 Veilleux S. et al., 2013, *ApJ*, 776, 27  
 Vogelsberger M., Genel S., Sijacki D., Torrey P., Springel V., Hernquist L., 2013, *MNRAS*, 436, 3031  
 Vogelsberger M., Sijacki D., Kereš D., Springel V., Hernquist L., 2012, *MNRAS*, 425, 3024  
 Wurster J., Thacker R. J., 2013, *MNRAS*, 431, 2513

out using  $10^7$  initial resolution elements, with all simulations estimating the fluid parameters at the full black hole smoothing length. These also show good agreement with each other, and good convergence with the comparable lower resolution run.

## APPENDIX A: THE BLACK HOLE SMOOTHING LENGTH

In Section 2.3.2 we described our procedure for calculating the fluid parameters in the vicinity of the black hole. In this appendix, we discuss the results of additional numerical tests we have carried out to demonstrate the robustness of this approach, which is commonly used in the literature.

To this end, we have run several simulations of our isolated disc galaxy (using  $10^5$  initial resolution elements) in which we vary the radius over which weighted averages of the fluid parameters are estimated, for the purposes of calculating the accretion rate. In all of these runs we enable black hole refinement, using our standard parameters. To ensure that the tests are consistent and to keep the tests as clean as possible we do not include black hole feedback of any type in these simulations. In Figure A1 we show the results of doing this for three runs where we estimate  $\rho_\infty$  and  $c_\infty$  at 1.0, 0.5 and 0.25 times the black hole smoothing length. The results show that both the measured quantities and the subsequently derived Bondi-Hoyle rate show good agreement for the duration of the black hole growth phase.

In addition, we also show the same simulations carried

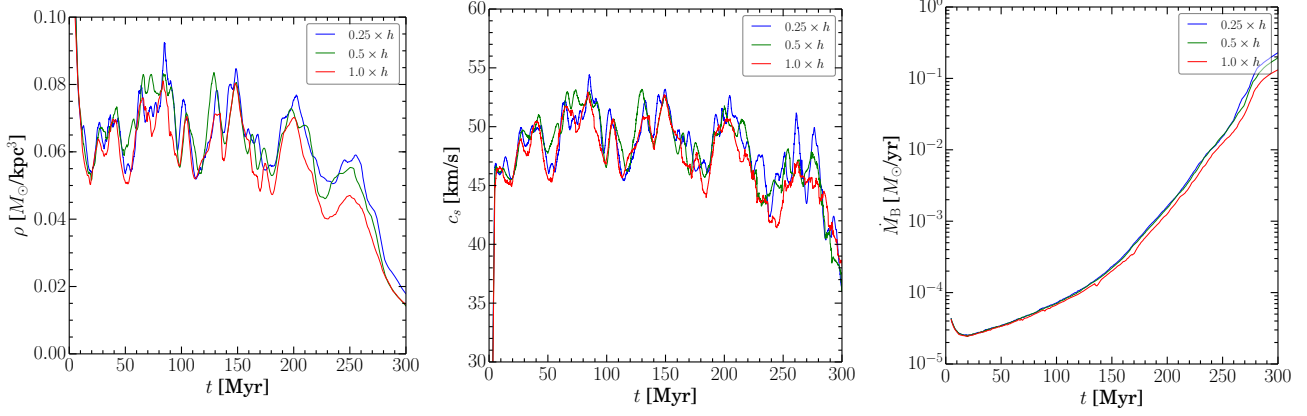


**Figure A1.** Fluid parameters and Bondi-Hoyle rate in simulations of an isolated disc galaxy ( $10^5$  initial resolution elements) and no black hole feedback. All runs include our black hole refinement scheme. Changing the radius over which we calculate the weighted average of the fluid parameters does not substantially effect our results.

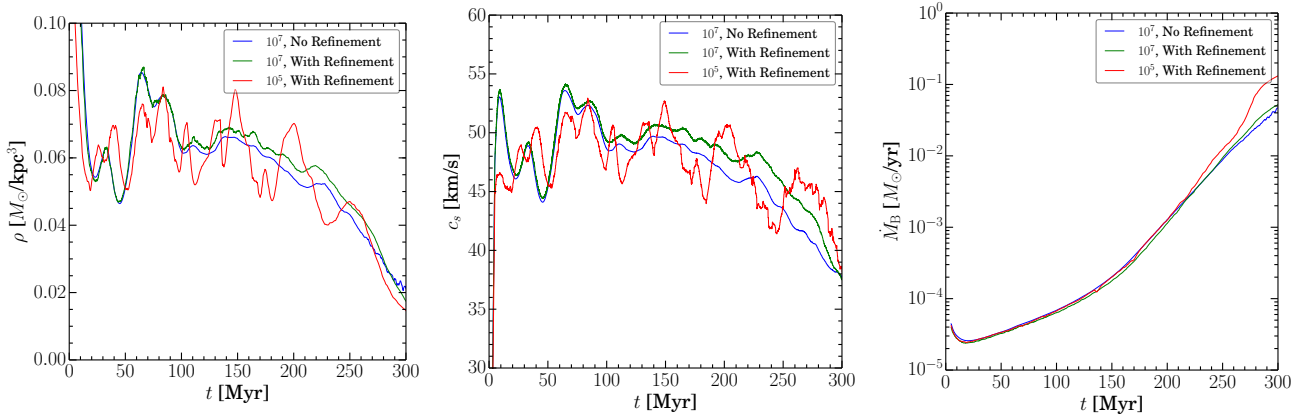


**Figure A2.** Convergence of refinement scheme. Here, we show the fluid parameters (estimated at the full smoothing length of the black hole) and Bondi-Hoyle rate in simulations of an isolated disc galaxy with no black hole feedback. We plot two high resolution runs using  $10^7$  resolution elements, with and without refinement, that show good agreement with each other, and also with the lower resolution run ( $10^5$  resolution elements) that includes black hole refinement.